NON-INVASIVE SEGMENTATION OF THE HUMAN LATERAL GENICULATE NUCLEUS

Kevin DeSimone

A DISSERTATION SUBMITTED TO THE FACULTY OF GRADUATE STUDIES IN PARTIAL FULLFILMENT OF THE REQUIREMENTS FOR THE DEGREE OF DOCTOR OF PHILOSPHY

GRADUATE PROGRAM IN PSYCHOLOGY
YORK UNIVERSITY
TORONTO, ON

JULY 2016

Abstract

The human subcortex contains multiple nuclei that govern the transmission of information to and among cortical areas. In the visual domain, these nuclei are organized into retinotopic maps. Because of their small size, these maps have been difficult to precisely measure using phase-encoded functional magnetic resonance imaging, particularly in the eccentricity dimension. Using instead the population receptive field model to estimate the response properties of individual voxels, I was able to resolve two previously unreported retinotopic maps in the thalamic reticular nucleus and the substantia nigra. I measured both the polar angle and eccentricity components, receptive field size and hemodynamic response function delay in the these nuclei and in the lateral geniculate nucleus, the superior colliculus, and the lateral and intergeniculate pulvinar. The anatomical boundaries of these nuclei were delineated using multiple averaged proton density-weighted images and were used to constrain and confirm the functional activations. Deriving the retinotopic organization of these small, subcortical nuclei is the first step in exploring their response properties and their roles in neural dynamics. I then extended the spatial pRF model to include model parameters for capturing temporal tuning properties of the LGN. The LGN is a laminar structure whose layers can be functionally differentiated based on the response properties of the neurons contained therein. This new spatiotemporal pRF model was designed to detect the differences in the temporal frequency tuning and neural discharge pattern of neurons among the magnocellular and parvocellular layers of the LGN. I then conducted two follow-up experiments where I functionally segment the layers of the LGN using a model-free data-driven approach. I compare the results of the pRF modeling to these model-free data-driven segmentations.

Table of Contents

List of Figures

List of Tables

Chapter 1: Introduction

Spatial Tuning of Subcortical Nuclei

The subcortex of the brain contains multiple nuclei that play critical roles in brokering the exchange of information among cortical areas (Sherman, 2007). For example, the subcortical visual system, including the LGN and pulvinar nuclei in the thalamus, and the superior colliculus (SC) in the brainstem, contains important hubs regulating the flow of visual information from the retina to cortex and are implicated in visual attention (Kastner et al., 2004; Schneider et al., 2004; Schneider, 2011; Arcaro et al., 2015). However, the human subcortical visual system remains poorly understood.

Using the phase-encoding retinotopic mapping approach, fMRI experiments in the human have corroborated the existence of detailed maps in the LGN (Schneider et al., 2004; Schneider and Kastner, 2009; Schneider, 2011), the SC (Schneider et al., 2005; Schneider and Kastner, 2005; Schneider, 2011), and the pulvinar (Cotton and Smith, 2007; Smith et al., 2009; Schneider, 2011). In these cases, the polar angle maps were most easily detected while the eccentricity measures were weak and the maps incomplete with respect to the electrophysiological results. In recent years,

the pRF model has been offered as a powerful alternative to the phase-encoding method for obtaining expressive and detailed maps of multiple visual areas throughout cortex (Dumolin and Wandell, 2008; Amano et al., 2009). The pRF model is a voxel-wise forward encoding approach that uses a spatially and temporally dynamic stimulus to derive receptive field properties from the BOLD signal emanating from a population of neurons contained within a single voxel. The pRF model is able to provide retinotopic maps containing information about both the location and dispersion of a receptive field with a single dataset whereas the phase-encoding approach requires separate datasets for the polar angle and eccentricity measures and cannot provide information about the RF size of each voxel. Here I used the pRF model to precisely measure the retinotopic organization, spatial tuning, and hemodynamic response function (HRF) delay parameters of known subcortical visual nuclei, and seek to identify additional unreported maps.

Temporal Tuning of the LGN

The LGN is the major thalamic station that mediates the exchange of information between the retina and primary visual cortex. Its topographic organization and the response properties of its neurons have been

extensively studied in nonhuman primates (Polyak, 1953; Kaas et al., 1972; Malpeli and Baker, 1975; Connolly and Van Essen, 1984). The LGN is typically organized into six layers, with each layer receiving input from the contralateral or ipsilateral eye and containing a retinotopic map of the contralateral hemifield. Furthermore, the layers of the LGN can be functionally differentiated based on the response properties of the neurons contained therein. The four dorsal layers of the LGN contain small [parvocellular (P)] neurons characterized by sustained discharge patterns and low contrast gain, while the two ventral layers contain large [magnocellular (M)] neurons characterized by transient discharge patterns and high contrast gain (Wiesel and Hubel, 1966; Dreher et al., 1976; Creutzfeldt et al., 1979; Shapley et al., 1981; Derrington and Lennie, 1984; Merrigan and Maunsell, 1993; Maunsell et al., 1999; Solomon et al., 2004).

While the structure and function of the macaque LGN has been extensively studied and characterized, study of the human LGN *in vivo* has proven difficult due its small size and deep location in the brain. Historically, the study of the human LGN had been restricted to the anatomical resection of the postmortem brain and has revealed a laminar organization similar to that found in the macaque (Kupfer, 1962; Hickey and Guillery, 1979). The LGN is somewhat unique in the visual pathway in that there is a clear

separation of structure and function at a spatial scale that is resolvable by contemporary functional imaging techniques. Therefore, it provides a unique opportunity for developing and testing models of neural function, visual perception, and information flow throughout the brain. For instance, one prevailing theory of dyslexia contends that a malfunction in the magnocellular system throughout the brain is responsible for the behavioral deficits observed in dyslexics (Stein, 2001; Stein and Walsh, 1997). A key test of this theory would revolve around the functional segmentation of the LGN *in vivo*. Recent attempts have been made to segment the LGN into its M and P subdivisions using fMRI (Denison et al., 2014; Zhang et al., 2015). In these experiments, researchers took advantage of the complementarity of the response properties of M and P neurons to differentially drive the BOLD activity during the presentation of various stimulus features (i.e., contrast, spatial frequency, temporal frequency, color sensitivity). Using a general linear model (GLM), the experimenters categorized voxels on basis of their response preference as gleaned from the regression coefficients for various stimulus properties. Voxels were classified as M or P depending on their BOLD response to magnocellular-preferred stimulus features (i.e., high contrast, low spatial frequency, high temporal frequency, achromatic) or to parvocellular-preferred stimulus features (i.e., low contrast, high spatial

frequency, high temporal frequency chromatic). These findings are problematic for a few reasons. First, the experimenters defined their regions of interest (ROI) using functional activation. This approach can lead to inaccuracies in defining the boundaries of the LGN and may result in the inclusion of neighboring and visually responsive tissue including the pulvinar, the triangular area, and blood vessels. Second, these experimenters relied on a multivoxel clustering approach that imposed assumptions about the ratio of magnocellular to parvocellular tissue in the LGN (80% P, 20% M). A better test of the efficacy of the functional segmentation of M and P would be to measure the ratio of M and P segments in the clustered LGN rather than to impose this constraint on the clustering procedure itself. Third, the response of each voxel is characterized in terms of regression coefficients and thus shares only a statistical relationship with the stimulus properties that drive the voxel activity in the first place. The pRF model parameters are stimulus-referred, and so the pRF model estimates are expressed in terms of the encoding stimulus. Thus, the pRF model can make specific predictions about the BOLD response to varied stimulus properties.

The goal of this experiment was to develop a spatiotemporal pRF model to capture the functional divergence between the M and P subpopulations of the LGN. Using a spatially encoding stimulus that varied in

its flicker frequency over time, I sought to characterize each voxel in terms of its temporal response and in doing so produce a functionally segmented LGN. The parameter estimate maps I measured indicate that this simple modification to the spatial pRF model is able to capture functional differences among the magnocellular and parvocellular layers of the LGN.

Chapter 2: General Methods

Subjects

Three subjects participated in the study (26–34 years of age; 2 males, 1 female). One subject was left-handed. The subjects were in good health with no history of psychiatric or neurological disorders, had normal or corrected-to-normal visual acuity, gave their informed written consent, and were compensated for their participation. The study was approved by the York University Human Participants Review Committee. All of the subjects participated in a grand total of 13 scanning sessions, including one anatomical and twelve functional scanning sessions over the course of four experiments. For each experiment, we collected a total of 30 functional scanning runs per subject. All of these data were collected over the course of three years, from 2013 through 2016.

Data Acquisition

Data were acquired in the York University Neuroimaging Laboratory with a 3T Siemens Trio MRI scanner (Siemens, Erlangen, Germany) using a 32-

channel head coil. Thirty functional series of 200 volumes each were acquired with 14 coronal slices (1.5 mm isotropic voxels with 0.5 mm gap between slices) and a gradient echo, echo planar sequence with a 128 square matrix leading to an in-plane resolution of 1.5 × 1.5 mm^2 [repetition time (TR), 1.5 s; echo time (TE), 42 ms; flip angle, 90°]. A partial Fourier factor of 7/8 was used to acquire an asymmetric fraction of *k*-space to reduce acquisition time. The posterior edge of the acquisition volume was aligned in the midsagittal plane with the posterior edge of the superior colliculus (SC). The subjects' heads were surrounded by foam padding to reduce head movements.

In addition to the functional scanning sessions, each subject submitted to an anatomical scanning session. During the anatomical session, a high-resolution T_1-weighted MPRAGE (spin-echo, TR = 685 ms, TE = 8.6 ms, flip angle = 75°, 256 square matrix) and 40 coronal proton-density weighted volumes (TR = 3 ms, TE = 26 ms, flip angle = 120°, 19–48 slices, 1–2 mm thick, 256 square matrix, 192 mm field view, 0.75 × 0.75 mm^2 in-plane resolution) were acquired. Each proton-density image was motion-corrected to a single proton-density image, from which a mean proton-density image was computed and up-sampled by a factor of 2. These images were aligned to the MPRAGE and used for drawing regions of interest.

Data Preprocessing

The first four volumes of each run were discarded. To compensate for subject head movement, the remaining volumes were registered to the eighth volume obtained during the session. In addition to motion-correcting the functional imaging data, I also employed a volume-censoring procedure (Power et al., 2012). The frame-wise displacement is an aggregate measure of the translational and rotational head-movement gleaned from the motion-correction transformation for each volume in the functional series. Volumes with a frame-wise displacement greater than 0.35 mm were flagged for censoring and so were not included in the mean functional series. Each subject's complete dataset was registered to a single space, meaning that each functional run, ROI label-set, and underlying anatomy shared a common geometry. This approach provided me with an organizational framework where each particular LGN voxel contains a number of measures collected from a series of scanning sessions and experiments. A high-pass filter was applied to the functional time-series to remove low frequency MR signal drift. Data were spatially resampled using 3D cubic interpolation to half the voxel size, resulting in a voxel dimension of 0.75×0.75 mm^3. No spatial smoothing was applied to the functional data.

Regions of Interest Drawing

Regions of interest (ROI) were hand-drawn for each subject using a combination of anatomical and functional data and with the guidance of a histological human brain atlas (Mai et al., 2008). ROI for the LGN, SC, and the thalamic reticular nucleus (TRN) were drawn using only the proton-density anatomical data. ROI for the intergeniculate pulvinar (IP) and lateral pulvinar (LP) were drawn using a combination of anatomical landmarks and functional topography. The ROI for the substantia nigra (SN) were drawn using the functional data thresholded at $r \geq .25$ and guided by anatomical landmarks while consulting a detailed human brain atlas.

Chapter 3: Spatial pRF Modeling in the Subcortex

Methods

The first experiment I conducted revolved around using the spatial pRF model to retinotopically map the visual nuclei of the subcortex.

Display and Response Hardware

The stimuli were generated on an iMac Intel i7 computer (Apple, Inc., Cuppertino, CA) using Matlab software (The Mathworks, Natick, MA) and Psychophysics Toolbox 3 functions (Brainard, 1997; Pelli, 1997). Stimuli for the spatial pRF mapping experiment were projected at a frame-rate of 60 Hz from a SV-6011 projector (Avotec, Inc., Stuart, FL) inside the scanner room onto a translucent screen located at the end of the scanner bore. Subjects viewed the screen at a total viewing distance of 38 cm through a mirror attached to the head coil. The screen subtended 36° of visual angle horizontally and 28˚ vertically. A fiber optic response box (Current Designs, Inc., Philadelphia, PA) was used to collect subject responses. A trigger pulse from the scanner, which was translated into a key press by the response box,

was used to synchronize the start of the stimulus presentation to the beginning of the image acquisition.

Visual Stimuli and Procedure

The stimuli consisted of a checkerboard-patterned bar whose elements reversed contrast with a period of 4 Hz. The bar subtended 13° of visual angle across its width and extended beyond the boundaries of the screen along its length. During a single run, the bar appeared at four orientations (0°, 45°, 90°, and 135°) and transited across 26° of the visual field along a trajectory perpendicular to the bar orientation, passing through the fixation point at the center of the display. Thus, each run was comprised of eight 30 s bar sweeps, with 30 s mean-luminance blank periods at the beginning and end of each run. Throughout each 5 min run, subjects engaged in an attention task at fixation. Subjects were instructed to respond via button press whenever the fixation dot changed color between red and green.

Spatial pRF Model Estimation

I modeled the response of each voxel in terms of a Gaussian population receptive field (Dumoulin and Wandell, 2008). The model yields two-dimensional Gaussians that vary in visuotopic location and extent from voxel to voxel. In addition to the three parameters of the Gaussian, I also included model parameters for capturing the delay of the hemodynamic response function (HRF) and the baseline of the BOLD signal. The delay parameter captures the time-to-peak and time-to-undershoot of the HRF. The HRF delay can be estimated simultaneously with the three spatial tuning parameters since each bar sweep was paired with a bar sweep in the opposite direction. The baseline model parameter ensures that both the modeled and the measured BOLD signal vary about the same global mean. Thus, the pRF model formulation is given as

$$R = \mu + \beta \times \int S(x, y, t) * G(x, y)\ dxdy$$

$$G(x, y) = e^{-\frac{(x_0 - x)^2 + (y_0 - y)^2}{2\sigma^2}}$$

where S is the stimulus and G is the Gaussian where x, y, and, σ describe its location and extent. The parameter β is a scaling factor to account for the arbitrary units of the BOLD response and describes the amplitude. The parameter μ accounts for the global mean of each voxel and serves as a

baseline correction. The goodness of fit between the model prediction and the measured BOLD signal was assessed via the residual sum of squared errors (RSS). The effective stimulus was down-sampled to a resolution of 5% of the original using a two-dimensional bilinear interpolation. The time-series of each voxel was fitted in a two-phase procedure. An adaptive brute-force search strategy was used to sparsely sample the model parameter space and the best fit of this was used as the seed point for a fine-tuned gradient descent error-minimization using the non-resampled stimulus. The gradient-descent procedure used was a downhill simplex algorithm (Fletcher and Powell, 1963) to fine-tune the parameter estimates. A linear regression between the predicted and actual fMRI signal was used to determine the activation threshold. To ensure the reliability of our model estimation results, I also performed a split-half analysis. Two voxelwise mean time-series were computed from 15 randomly assigned and mutually exclusive runs from the 30 total runs collected from each subject. Model fits were estimated for each of these independent mean time-series and compared for consistency.

Neural Receptive Field Simulation

Each voxel in fMRI data may contain over a million individual neurons, each with its own visual receptive field (RF). The pRF model is meant to approximate the aggregate population response of the underlying neural RFs contained within a voxel. The measured pRF of a voxel, then, represents the sum of the RFs of the neurons contained within it. Thus, pRF size estimate derives from both the sizes of the neural RFs within a voxel as well as from the local visuotopic gradient. If a voxel contained an impossibly homogenous population of neurons with RFs all of the same size and centered on the same visuotopic location, then the pRF would be equivalent to neural RF. In reality, a voxel contains a population of neurons whose RFs vary in terms of extent and location. I sought to attenuate the influence of the local visuotopic gradient upon the measured pRF size. The distribution of RF centers and sizes within a pRF has been discussed previously (Smith et al., 2001; Jancke et al., 2004; Dumoulin and Wandell, 2008; Haak et al., 2012), but no one has attempted to infer the relative contributions of the intrinsic RF size and the visuotopic scatter from the measured pRF size. Here I use the local visuotopic gradient to estimate the distribution of RF centers within a voxel and, through simulation, estimate the RF size that best accounts for the observed

pRF size. The local visuotopic gradient was estimated to be one half of the mean visuotopic distance between the pRF center of a given voxel and the centers of its six nearest neighbors in brain volume space. Through simulation, I derived the smallest possible neural RF size—given the local visuotopic gradient—that would obtain the measured pRF size. Such an approach effectively deconvolves the local visuotopic gradient from the pRF size estimate. The simulated neural RF size was estimated by iteratively minimizing the RSS between the measured pRF receptive field and the sum of each set of simulated neural receptive fields. At each iteration, one thousand neural RFs centers were sampled from a uniform distribution spanning the measured local visuotopic gradient. Subject eye and head movements may also contribute to the pRF size estimates (Dumoulin and Wandell, 2008), but I do not consider these two factors beyond the volume-censoring procedure described in a previous section.

Results

Spatial pRF Estimates in the LGN and SC

Table 1. The mean volume ± subject-wise SEM for six subcortical nuclei.

	Left hemisphere	**Right hemisphere**
LGN	214 ± 1	229 ± 30
SC	342 ± 50	335 ± 47
LP	460 ± 39	636 ± 109
IP	174 ± 17	272 ± 45
TRN	505 ± 134	531 ± 132
SN	166 ± 89	78 ± 35

Table 1 shows the mean volumes for the ROI among our subjects, divided by hemisphere. Anatomically guided tracings of the LGN, the SC, and the TRN are shown in Figures 1 and 2 for a two subjects overlaid on top of the proton-density image. The use of proton-density images to guide the drawing the LGN ROI was critical, as the T1-weighted anatomical images did not offer sufficient contrast to identify the boundaries of the LGN. Use of functional data to determine the boundaries of the LGN causes overestimation of the LGN volume, as there are other retinotopically organized subcortical nuclei and draining veins nearby whose BOLD signal covaries with the visual stimulus.

I found clear, bilateral retinotopic maps in the LGN of all our subjects using the pRF model. Panels A and B of Figure 3 show the activation maps of two representative subjects. Activated voxels whose fMRI time-series correlated with the modeled time-series, $r \geq 0.25$, are shown. The zoomed activation maps are overlaid on PD scans, with the LGN highlighted with a

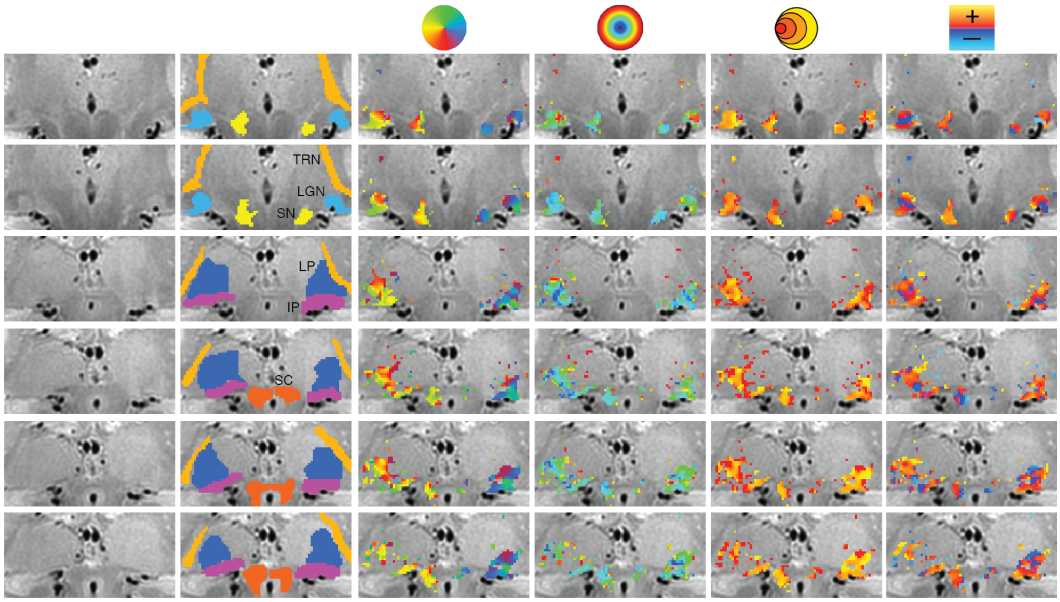

Figure 1. Detailed maps of the population receptive field estimates in across multiple subcortical nuclei. The proton density and regions of interest are shown (LGN, lateral geniculate nucleus; TRN,thalamic reticular nucleus; SN, substantia nigra; IP, intergeniculate pulvinar; LP, lateral pulvinar; SC, superior colliculus)

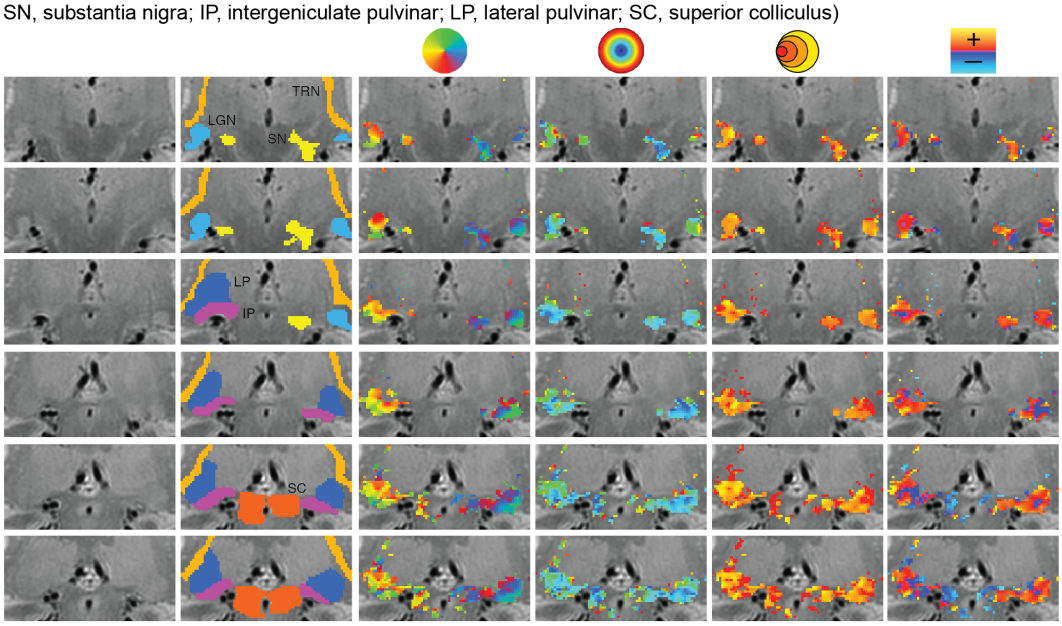

Figure 2. Maps of the pRF estimates in a second subject. Conventions as in Figure 1.

red square. The top and bottom panels show four coronal slices taken from each hemisphere and samples the activation maps along the anterior-to-posterior dimension. The columns of in Figure 3 shows the sliced-wise maps

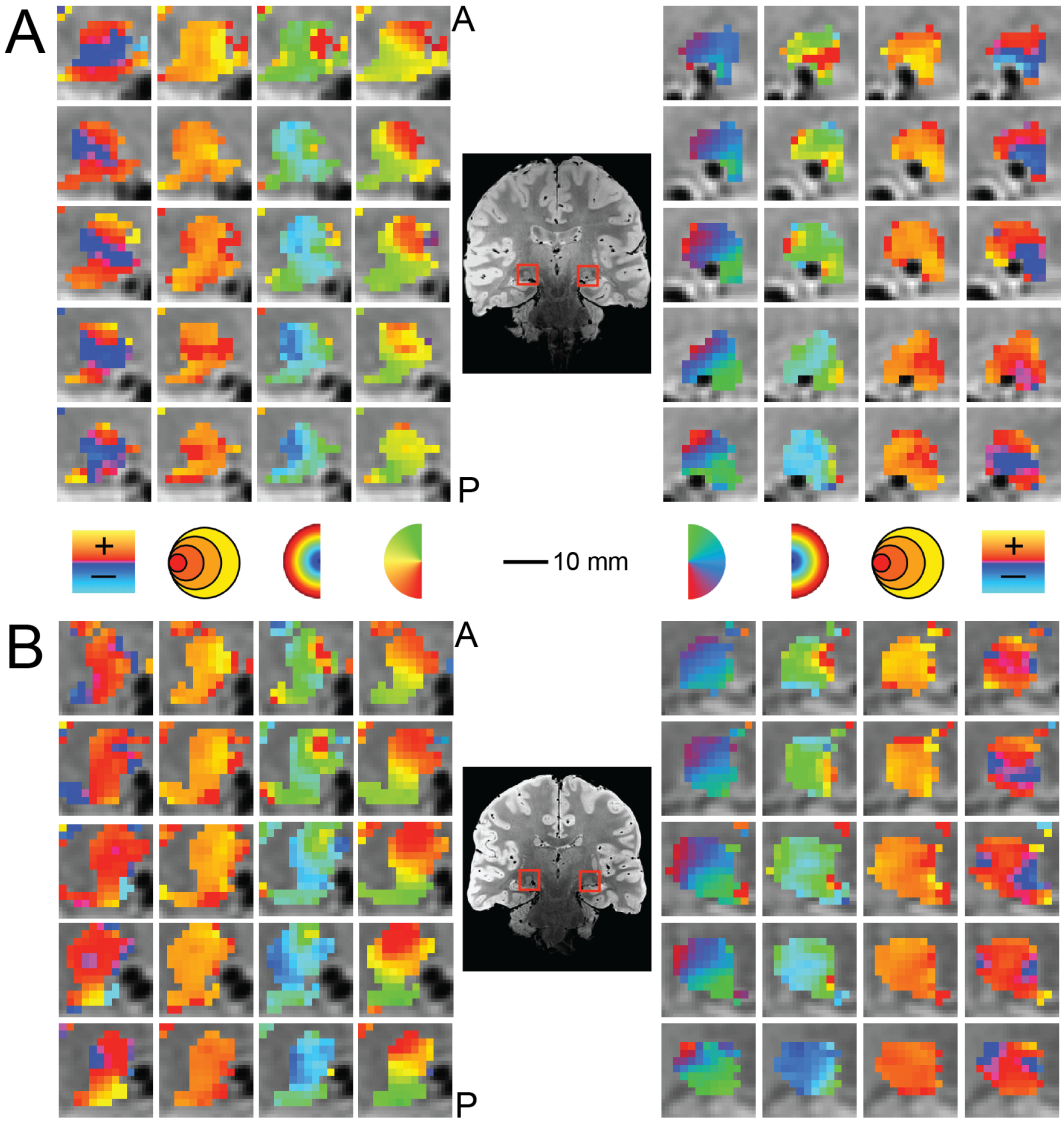

Figure 3. Detailed maps of the pRF estimates in the LGN. The model estimates are overlaid on the proton-density image for the left and right LGN. Separate subjects are shown in panels A and B. Columns illustrate the polar angle, eccentricity, pRF size, and HRF delay estimates.

for each of the pRF model parameters (polar angle, eccentricity, receptive field size, and HRF delay). The polar angle and eccentricity measures were calculated using the pRF location estimates initially derived in Cartesian coordinates. In both subjects shown, the polar angle maps had the same

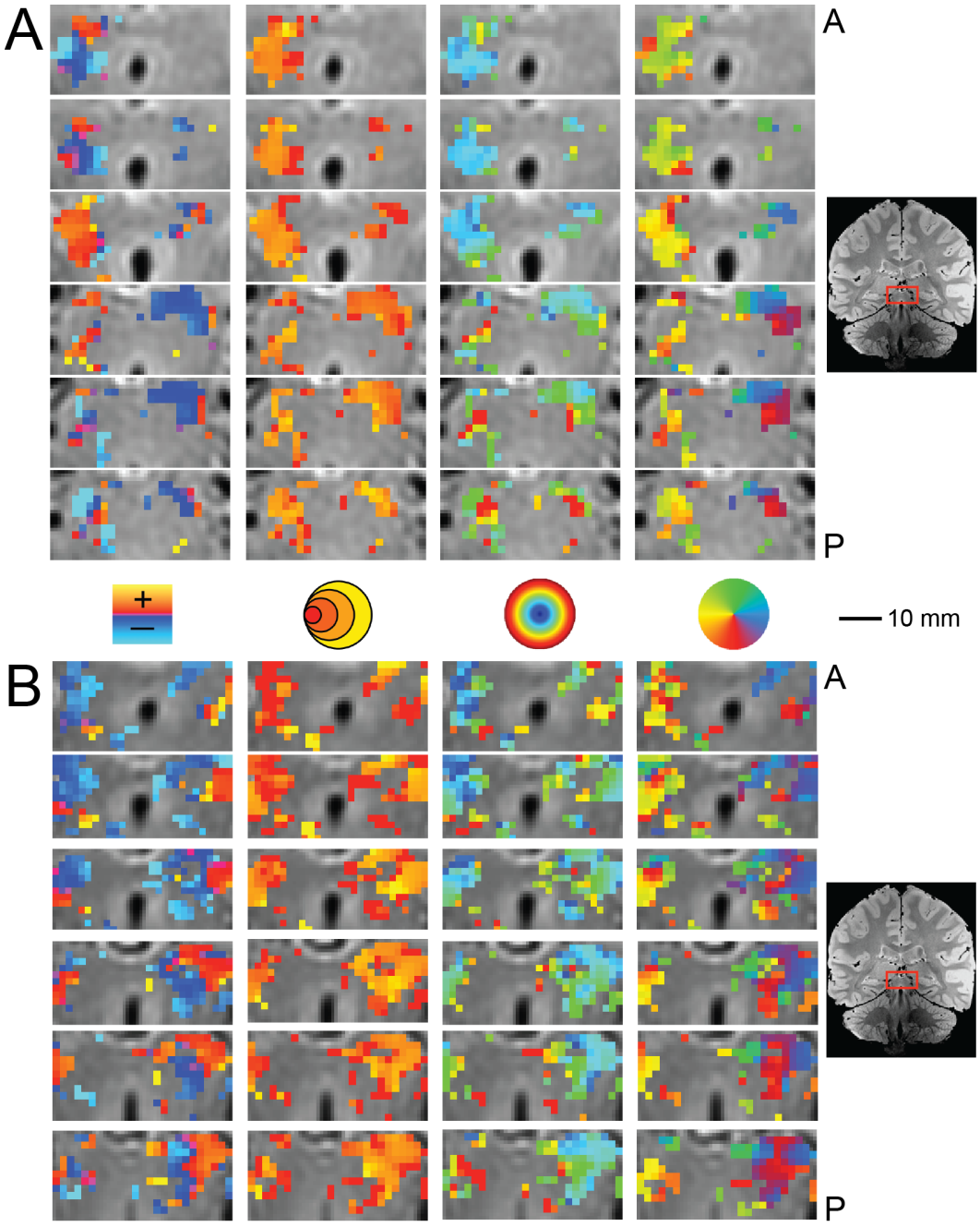

Figure 4. Detailed maps of the pRF estimates in the SC in two subjects. Conventions as in Figure 2.

anatomical orientation whereby representations of the upper vertical meridian were represented in the inferior and lateral portions of the LGN,

the lower vertical meridian was represented in the superior and medial portion of the LGN, and the horizontal meridian was oriented at a roughly 45° angle, dividing the upper and lower visual field representations. The eccentricity maps among our subjects showed a similar consistency in the pattern of activation. Here, I found an anterior-to-posterior gradient whereby foveal representations were found near the posterior end of the LGN and more peripheral representations were found near the anterior end of the LGN. Likewise, the pRF size maps showed a similar anterior-to-posterior gradient whereby smaller pRF sizes were found near the posterior end of the LGN and larger pRF sizes were found near the anterior end of the LGN.

I also found robust and retinotopically organized activations maps in the SC using the pRF estimation method. Figure 4 shows the activation maps for each of the pRF model parameters in successive coronal slices of the brainstem of two representative subjects. Again, I found orthogonal representations of polar angle and eccentricity along in the SC of each of our subjects, best viewed in the coronal plane. There was a consistent medial representation of the upper vertical meridian and lateral representation of t he lower vertical meridian, with a representation of horizontal meridian oriented at roughly 45°, dividing the upper and lower contralateral hemifield

representations. I found a foveal-to-periphery representation gradient for eccentricity along the anterior-to-posterior anatomical direction. Again, the

eccentricity; that is, smaller pRF sizes were found toward the superior-lateral portion of the SC while larger pRF sizes were found toward the inferior-medial portion of the SC.

Spatial pRF Estimates in Other Subcortical Nuclei

In addition to the LGN and SC, I found a number of other subcortical nuclei whose functional time-series was driven by the moving bar stimulus and from which I could compute reliable pRF estimates across subjects. Figures 1 and 2 show the activations maps of each of the four pRF model estimates. from two representative subjects, with the displayed maps spanning a series of non-consecutive coronal slices and overlaid on a broader anatomical window. The two leftmost columns show the unlabeled anatomical and the anatomical with overlaid ROI to illustrate the voxels that were selected for further analysis.

The IP and LP can be differentiated from one another in part based on a shared representation of the fovea. Bilaterally, the IP and LP shared a foveal

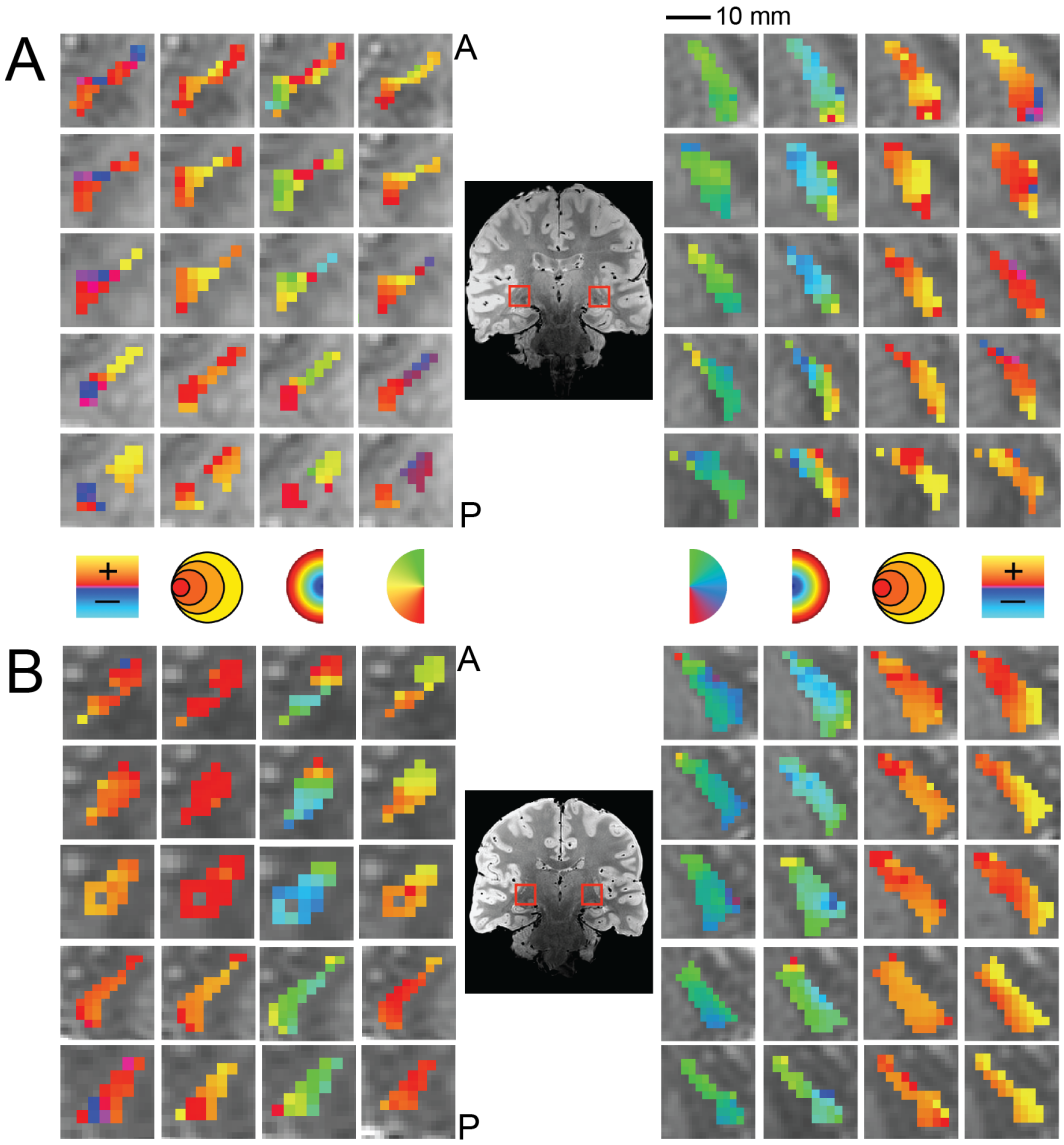

Figure 5. Detailed maps of the pRF estiamtes in the TRN of two subjects. Conventions as in Figure 3.

eccentricity representation running along an inferior-lateral to superior-medial direction oriented at about 45° to the midsagittal plane. In addition, these two pulvinar nuclei showed an anterior-posterior eccentricity representation gradient whereby foveal representations were found more anteriorly and peripheral representation more posteriorly. The polar angle

maps in the IP and LP were found to be orthogonal to the corresponding eccentricity maps. For both the IP and LP, the upper vertical meridian was represented inferiorly and laterally while the lower vertical meridian was represented superiorly and medially. The topography of the eccentricity and polar angle maps was found bilaterally among our three subjects.

I also found retinotopic maps in the TRN among our subjects (Figure 5). The TRN runs along the transverse length of the thalamus and wraps around the lateral surface of a number of thalamic structures including the pulvinar and the LGN. The structure of the TRN was identified anatomically on the proton-density images. The TRN showed an anterior-posterior and medial-lateral gradient of polar angle representation with the upper vertical represented more anteriorly and medially while the lower vertical meridian represented more posteriorly and laterally. The eccentricity map of the TRN was oriented along an inferior-superior axis with a foveal representation near the inferior end of the TRN and a peripheral representation near the superior end of the TRN. Only a small subset of voxels in the anatomically defined TRN ROI showed a retinotopic organization. The portions of the TRN that did show retinotopic maps were clustered around the other visually evoked nuclei of the thalamus including the LGN and the pulvinar.

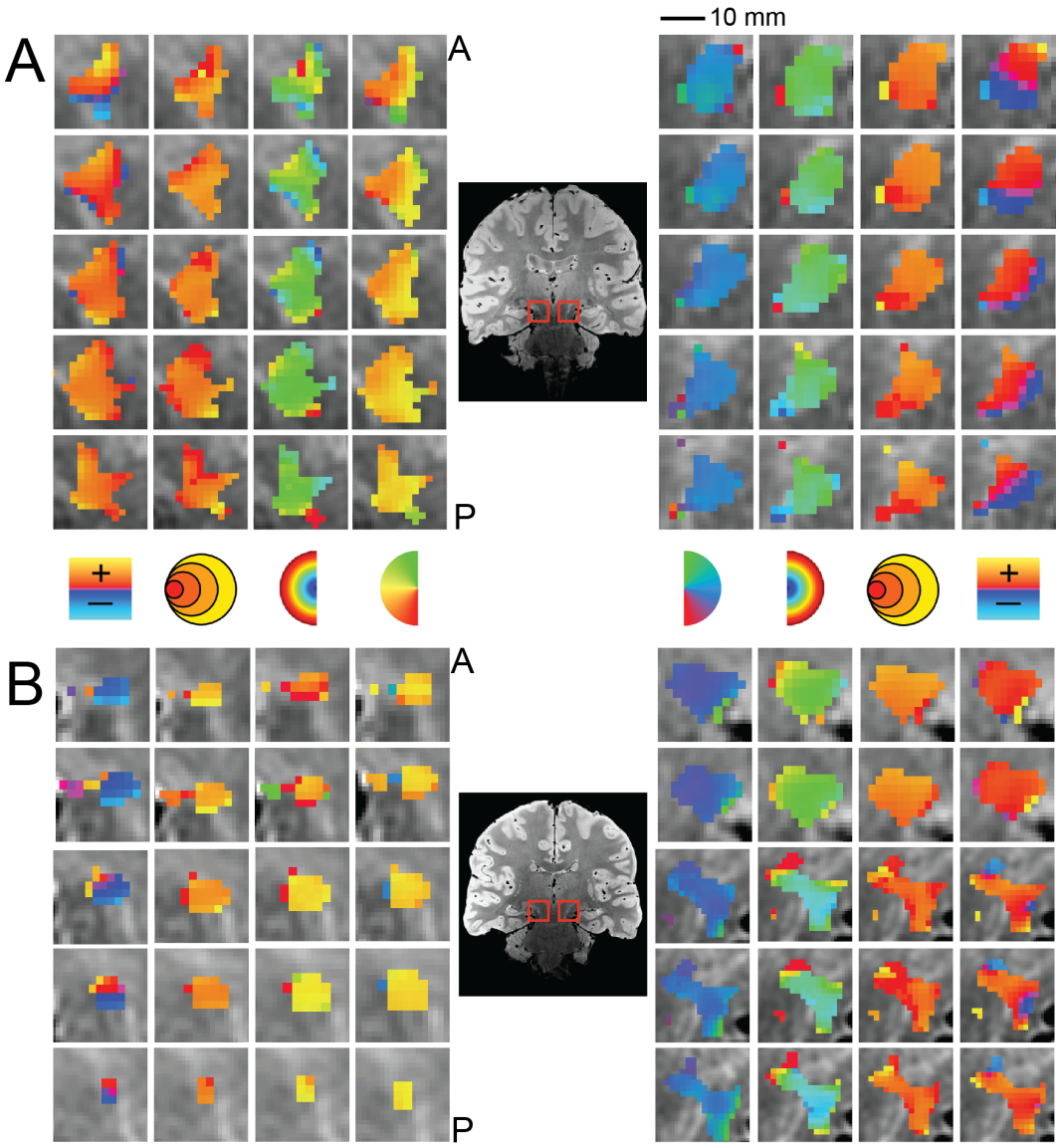

Figure 6. Detailed maps of the pRF estiamtes in the SN of two subjects. Conventions as in Figure 3.

I also found bilateral retinotopically organized maps that I determined to be part of the SN (Figure 6) by comparison of our proton-density images

with a histological atlas (Mai et al., 2008). The SN polar angle representations were organized along a medial-to-lateral direction with the upper vertical meridian represented more medially and the lower vertical meridian represented more laterally. The eccentricity maps were organized along an anterior-to-posterior direction with more foveal representation in the anterior SN and more peripheral representation in the posterior SN. The retinotopic map I found in the SN is most likely the pars reticulata of the SN (Hikosaka and Wurtz, 1983a).

Figure 7 shows a comparison of the pRF model parameter estimates pooled across the three subjects for each of the six subcortical nuclei. Panel A shows the polar angle representations among the various subcortical visual nuclei. Here, I plot the fractional volume as a function of polar angle for each hemisphere separately, using sixteen 22.5° radial segments. All subcortical nuclei activated bilaterally and showed a strong contralateral representation of the visual space. Additionally, all areas showed a representational bias such that the horizontal meridians were overrepresented and the vertical meridians were underrepresented. This representational bias has been previously reported in the LGN, the SC, the IP, and the LP (Schneider et al., 2004; Schneider et al., 2005; Schneider and Kastner, 2009; Schneider, 2011). The TRN showed the most ipsilateral representation of polar angle among

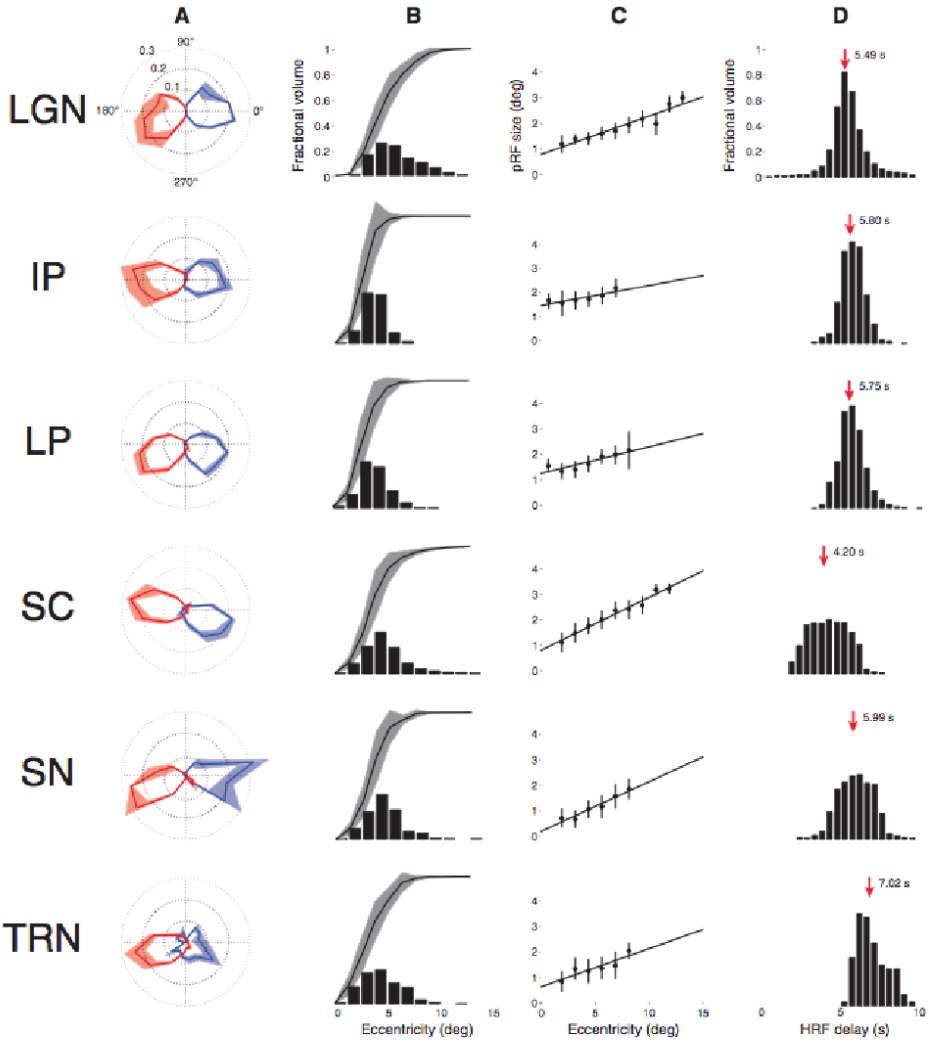

Figure 7. Model parameters for each of the six subcortical nuclei across three subjects. A, polar angle plots for six subcortical nuclei. The left (blue) and right (red) hemispheres are plotted separately. The solid line shows the mean fractional volume at any given polar angle. The shaded region shows the standard error of the mean. B, eccentricity measures among the six subcortical nuclei. The black bars represent the fractional volume at each degree of eccentricity from fixation. The solid black lines represent the cumulative sum of the fractional volume at each degree of eccentricity from fixation. The shaded regions represent the standard error of the mean. C, pRF sizes versus eccentricity in each of the six subcortical nuclei. The mean pRF size is shown at each 1˚ eccentricity bin, along with the standard error of the mean. The solid black lines show the linear fits of the plotted data-points. Eccentricities with fewer than 5 data-points are not shown. D, HRF delay measures among the six subcortical nuclei. The black bars represent the fractional volume at each HRF delay. The solid black line represents the cumulative sum of the fractional volume at each HRF delay.

the

six subcortical nuclei sampled, replicating previous findings of interhemispheric activation in the TRN (Viviano and Schneider, 2015). Panel B of Figure 7 communicates another somewhat unique feature of the structure of the retinotopic organization in the TRN. Here, we've plotted the fractional volume of each ROI as a function of eccentricity. The LGN, SC, SN, and TRN all show about 50% of their volumes represented the central 5° of the visual field, with the remaining ROI volume representing the next 10° of eccentricity. The IP and LP showed slightly steeper curves where about 50% of their volumes represented the central 2–3° of the visual field.

The structure of the retinotopic maps among the six subcortical nuclei is further illustrated in panel C of Figure 7. Here, the receptive field sizes among the voxels of each ROI are plotted as a function of eccentricity. Each filled black circle represents the mean receptive field size binned at 1° segments of eccentricity, along with the standard error of the mean in black bars. Eccentricities with fewer than five receptive field estimate measures were excluded. The linear fit among all data-points is shown with a solid black line. In all ROI, I found a positive relationship between pRF size and eccentricity, with RF size increasing with eccentricity as has been demonstrated in brain imaging studies using a similar model in cortex (Dumoulin and Wandell, 2008; Amano et al., 2009).

Because the visual stimulus was composed of opposing bar sweeps through the visual field, I was able to model the HRF delay of each voxel in addition to the spatial parameters of the pRF model. The HRF delay estimates are shown for each of the six subcortical nuclei in panel D of Figure 7. For each voxel, the HRF delay parameter was computed as the time-to-peak (and time-to-undershoot, not shown) of the canonical double-gamma HRF (Friston et al., 1998; Glover, 1999; Worsley et al., 2002). The mean HRF delay for each of the subcortical nuclei is shown as well. The SC was found to have a mean HRF delay of 4.20 s, while the distributions of the mean of the rest of the ROI were all greater than 5 s. Notably, even though the TRN showed a mean HRF delay of 7.02 s.

Figure 8 shows the results of the split-half model estimation. Two mean time-series were computed from 15 randomly assigned mutually exclusive runs from the 30 total runs collected from each subject. Model fits were estimated for each of these independent mean time-series and compared in panels A through D in Figure 8. The results of the model estimation for first (black) and second (red) halves of the data are very similar across ROI and metrics. The most notable difference between these results from each 15 run half of the dataset and the results for all 30 runs in Figure 6 is the TRN polar angle plot. Reducing the number of runs to one half

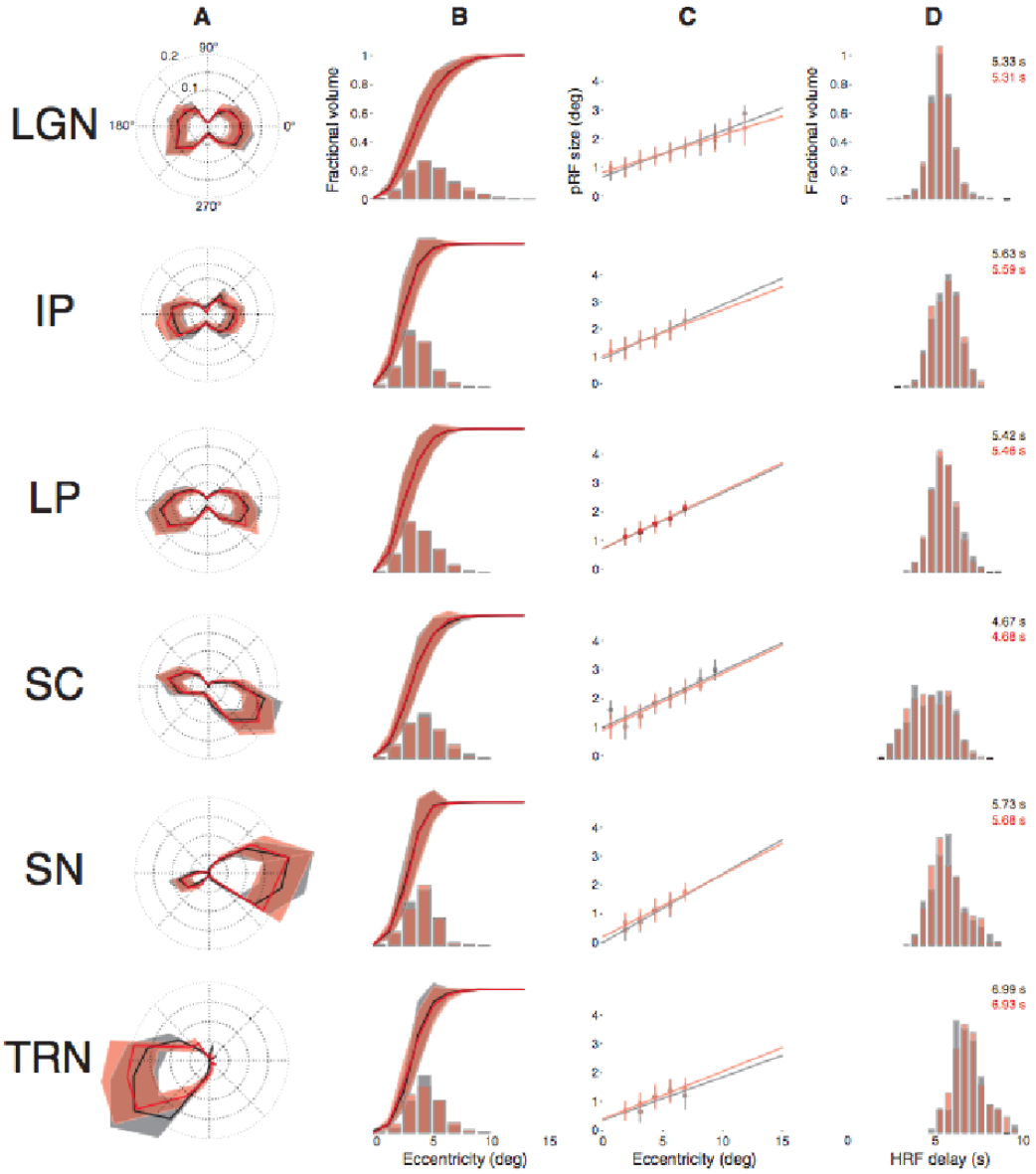

Figure 8. To estimate the reliability of the data, we show the model parameter estimates for two independent halves of the data (red and black). Conventions as in Figure 6.

the total data collected resulted in a loss of the TRN representation in the left visual field. This suggests that the signal-to-noise in the TRN is lower than in the other five subcortical nuclei.

Neural Receptive Field Simulation

The results of the neural RF simulation are shown in Figure 9. Here, I plot the estimated pRF size versus simulated RF size for each voxel across the six subcortical nuclei. Points falling below the line of identity (red) have neural RF sizes that are smaller than the pRF size, which indicates the effect of the local visuotopic gradient in inflating the pRF size. Voxels with pRF sizes <5° exhibited the largest effects.

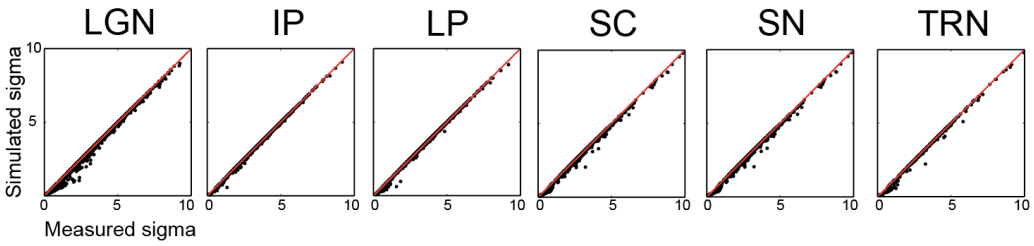

Figure 9. RF versus pRF size among the six subcortical nuclei. The simulated neural RF size is plotted as a function of the measured pRF size for each voxel, across subjects. The red line indicates identity.

Chapter 4: Extending the pRF Model to the Temporal Domain

Methods

Having shown that the standard Gaussian pRF model (Dumoulin and Wandell, 2008) can be used to estimate the spatial tuning of a number of subcortical visual nuclei, I turned my sights on extending to the temporal domain. This approach was aimed at differentiating the magnocellular and parvocellular layers of the LGN based on their temporal frequency tuning and neural discharge patterns.

Display Hardware

The stimuli were generated on a Mac Pro i7 computer (Apple Inc., Cupertino, CA) with a NVIDIA Quadro 4000 video card, using Matlab software (The Mathworks, Natick, MA) and Psychophysics Toolbox 3 functions (Brainard, 1997; Pelli, 1997). Stimuli were presented using a VPixx ProPIXX DLP LED projector (Saint-Bruno, QC, Canada) located outside the scanner room and projected through a wave-guide and onto a translucent screen located at the end of the scanner bore. Subjects viewed the screen at a total viewing

distance of 31 cm through a mirror attached to the head-coil. The display subtended approximately 26˚ of visual angle horizontally and 20˚ vertically. The ProPIXX projection system has a native resolution of 1920 × 1080 and a refresh rate of 120 Hz. This projector can be run in a quadrature mode whereby the resolution of the display is quartered while the refresh rate is quadrupled. Thus, we presented the stimulus at pixel resolution of 960 × 540 and at a temporal refresh rate of 480 Hz. (120 Hz × 4 spatial quadrants). A trigger pulse from the scanner, which was translated into a key press by the response box, was used to synchronize the start of the stimulus presentation to the beginning of the image acquisition.

Visual Stimuli and Procedure

The stimulus consisted of a uniform bar subtending 5˚ of visual angle across its width and extending to the display boundary along its length. The bar transited across the visual field in four directions (0˚, 90˚, 180˚, 270˚) twice during each scanning run (Figure 10). The luminance of the bar was sinsuoidally modulated between black and white at a rate of 10 Hz for the first four passes and at 20 Hz for the second four passes. The 10 Hz and 20 Hz luminance profiles were sampled and displayed at 480 Hz so as to smoothly

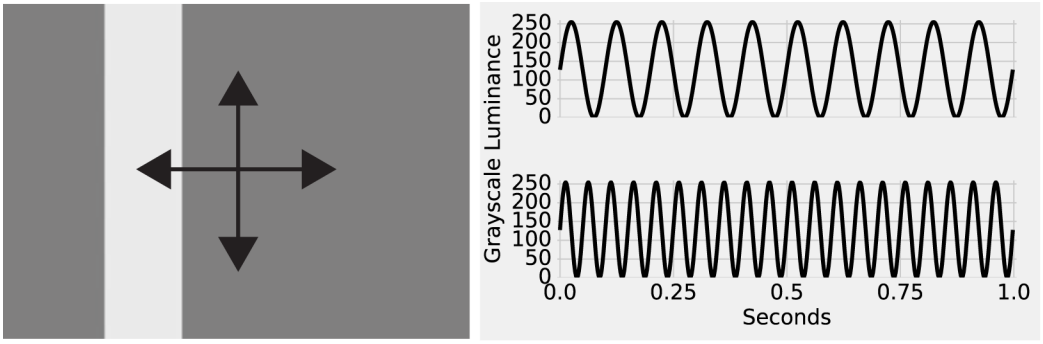

Figure 10. Sweeping bar stimulus. The uniform flickering bar swept across the display 8 times in 4 directions and at 2 flicker frequencies, 10 Hz and 20 Hz.

sample the sinusoidal luminance modulation. The bar stimulus was presented overtop a uniform mean luminance (i.e., gray) field while subjects fixated a central dot. Each run lasted 5 minutes.

Spatiotemporal pRF Model Estimation

I modeled the BOLD signal of each voxel in terms of a spatiotemporal population receptive field. The spatial response of each voxel was characterized as a two-dimensional Gaussian in visuotopic coordinates (Dumoulin and Wandell, 2008). It describes the location and extent of the BOLD response of a given voxel, formulated as

$$R = \mu + \beta \times \int S(x,y,t) * G(x,y)\ dxdy$$

$$G(x,y) = e^{-\frac{(x_0-x)^2+(y_0-y)^2}{2\sigma^2}}$$

where S is the stimulus and G is the Gaussian where x, y, and, σ describe its location and extent. The parameter β is a scaling factor to account for the arbitrary units of the BOLD response and describes the amplitude. The parameter μ accounts for the global mean of each voxel and serves as a baseline correction. To this spatial pRF model, I added a temporal component to capture the differences in the discharge pattern among the magnocellular and parvocellular neural subpopulations of the LGN. Among their many complimentary stimulus response properties, magnocellular and parvocellular neurons of the macaque LGN have been shown to functionally diverge on basis of the transience of their responses (Maunsell et al., 1999; Solomon et al., 2004), where parvocellular neurons show a sustained response to a light stimulus while magnocellular neurons show a transient response. Thus, the temporal pRF model component approximates the transience and sustainability of the BOLD response of a given voxel to a flickering visual stimulus. I modeled the sustained response as one-dimensional Gaussian in time, formulated as

$$R_S(t) = e^{-\frac{(t_0-t)^2}{\sqrt{2\pi\tau}}}$$

$$R_T(t) = R_S{}'$$

where the sustained response R_S is a one-dimensional Gaussian spanning the duration of a single volume acquisition, is centered at time t, and has a

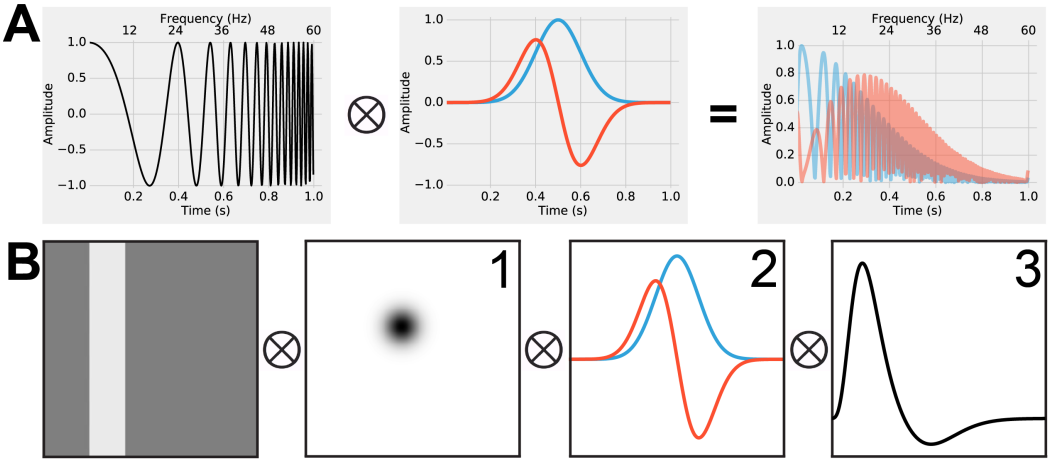

Figure 11. The spatiotemporal pRF model. **A**, Temporal receptive fields. A frequency modulated chirp stimulus (left panel) is convolved with a Gaussian temporal receptive field (sustained RF, blue) and its first derivative (transient RF, red). The amplitude of the chirp passed through the sustained RF is higher at low frequencies compared to the transient RF. At higher frequencies, the amplitude of the transient response is higher compared to the sustained response.**B**, Generating a model response. The binarized sweeping bar stimulus is passed through three convolutions. The spatial response is extracted (1) and passed through the sustained (blue) and transient (red) temporal receptive fields (2).These signals are then linearly combined according to the weight parameter. This weighted sum of the transient and sustained responses is then convolved with the hemodynamic response function (3). The modeled response is then regressed against the measured BOLD.

dispersion τ in time. The transient response R_T is simply taken to be the first derivative of the sustained response R_S. Figure 11A illustrates the behavior of the temporal receptive fields when convolved with a frequency modulated chirp stimulus. When the stimulus is convolved with the sustained (blue) and transient (red) temporal receptive fields, the relative amplitude of the resulting signals varies according to the frequency. The sustained response has a large amplitude at low frequencies but the attenuates as the frequency increases, and the transient response has a small amplitude at low frequencies and becomes larger as the frequency increases. Thus, the information about the temporal frequency tuning can be recovered from the amplitude modulation of modeled response. However, since there can only be one measured response from each voxel over time, it is necessary to combine the output of the sustained and transient temporal receptive fields.

To accomplish this, I added a weight parameter for mixing the sustained and transient responses to produce a weighted sum. Owing to the relatively coarse sampling resolution of fMRI and the small size of the LGN and its laminar subdivisions, it is exceedingly unlikely that any given voxel will sample from a purely magnocellular or parvocellular population of neurons. Thus, I included in the model a term for mixing the transient and sustained temporal components for estimating the measured BOLD response. With this term and the spatial and temporal model components, the full spatiotemporal pRF model is given as

$$R = \mu + \beta \times \int S(x, y, t) * G(x, y) * (\omega * R_S(t) + (1 - \omega) * R_T(t)\, dxdydt$$

where the modeled BOLD response R is taken to be the integral of the stimulus S, the Gaussian spatial receptive field G, the sustained and transient temporal receptive fields R_S and R_T, the mixing parameter ω, the scaling parameter β, and the baseline parameter μ. Thus, the model has three parameters (x, y, σ) describing the spatial tuning and one parameter (ω) describing the temporal tuning of each voxel.

In addition to these model parameters, I also included model parameters for capturing the delay of the hemodynamic response function (HRF) and dispersion of the temporal RF across the LGN within a single subject. I estimated the HRF delay parameter δ and the temporal RF

dispersion parameter τ simultaneously among all voxels in a yoked fashion, so that while the 6 spatiotemporal pRF model parameters $(x, y, \sigma, \omega, \beta, \mu)$ were estimated independently for each voxel in a given subject's LGN, the model parameters δ and τ were estimated iteratively and in tandem. Thus, all voxels shared the same HRF delay and temporal RF dispersion at each iteration of the gradient-descent procedure. The spatial response was convolved with the R_S and R_T temporal receptive fields, which in turn were combined according to the mixing parameter ω and convolved with the HRF (Figure 11B).

The goodness of fit between the model prediction and the measured BOLD signal was assessed via the residual sum of squared error (RSS). The time-series of each voxel was fitted in a two-phase procedure. The first phase consisted of a sparse and coarse global grid-search that adaptively constrained the search boundaries. The effective stimulus was down-sampled to a resolution of 5% of the original, using a two-dimensional bilinear interpolation. An adaptive brute-force search strategy was used to sparsely sample the model parameter space and the best fit of this was used as the seed point for a fine-tuned gradient descent error-minimization using the non-resampled stimulus. The gradient-descent procedure used was a downhill simplex algorithm (Fletcher and Powell, 1963) to fine-tune the

parameter estimates. A linear regression between the predicted and the measured BOLD signal was used to determine the activation threshold.

Results

Spatiotemporal pRF model estimates

Table 2 shows the mean volumes for the LGN ROI among our subjects, divided by hemisphere. The use of PD images to guide the drawing of the LGN ROI was critical, as the T1-weighted anatomical images did not offer sufficient contrast to identify the boundaries of the LGN. Table 1 also shows the activated volumes among our subjects and hemispheres, discounting voxels that did not survive the activation threshold ($r^2 > .10$) computed by regressing the measured BOLD response against the modeled pRF response.

	Left hemisphere	Right hemisphere
LGN	255 ± 14	251 ± 22
LGN, $r^2 > .10$	69 ± 2	65 ± 6

Table 2. The mean volume of the left and right LGN ± subject-wise SEM. Also shown are the mean activated volumes after statistical thresholding.

I found clear bilateral retinotopic maps in the LGN of each of our three subjects. Figure 12 shows the pRF model parameter maps for two subjects (panels A and B). Each panel is subdivided into columns representing the pRF model parameters and rows representing sequential coronal slices through the LGN. I converted the location parameters from Cartesian to polar coordinates. Thus, the columns of panels A and B show model estimates for the polar angle, eccentricity, receptive field size, amplitude, and weight parameters. In addition, I also show the unlabeled PD image for each slice to highlight the clarity that the PD image affords in determining the location and extent of the LGN. Only voxels exceeding the activation threshold are shown in the functional maps. The retinotopic organization of the subjects shown in panels A and B of Figure 12 are in close agreement with our previous findings with the spatial pRF model (Figure 3). Each LGN contains a representation of the contralateral hemifield, with upper vertical meridian represented along the inferior-lateral boundary of the LGN, the lower vertical meridian represented along the superior-medial boundary of the LGN, and the representation of the contralateral horizontal meridian oriented at approximately 45˚ subdividing the upper and lower visual field representations in each LGN. Figure 13A shows the polar angle representation of the LGN pooled among our three subjects. Here, I plot the

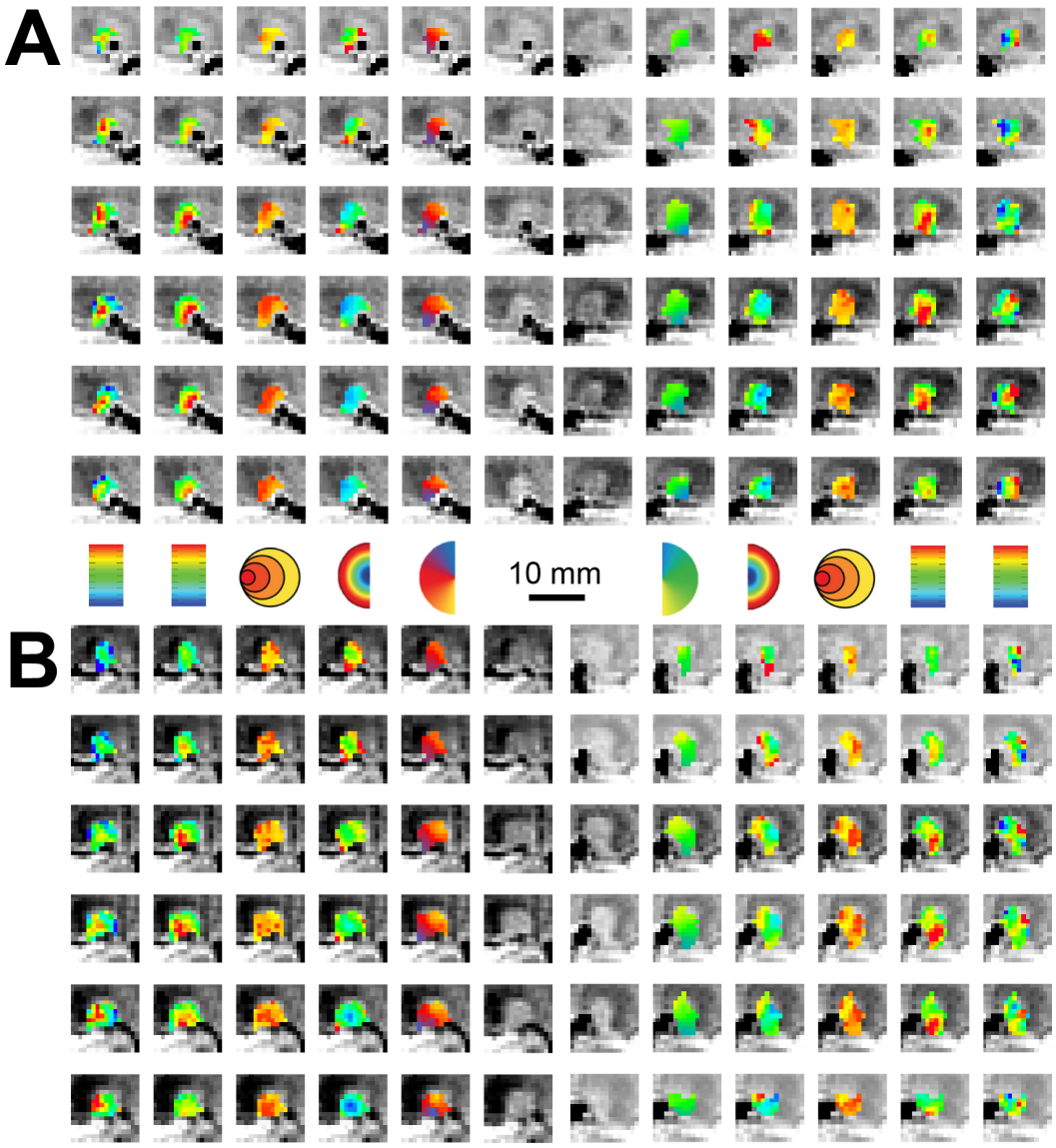

Figure 12. Detailed model parameter estimate maps in the human LGN. **A**, Parameter estimates overlaid atop the PD image for both the left and the right LGN for a single subject. The innermost columns show the unlabeled PD image, followed by the polar angle, eccentricity, receptive field size, amplitude, and weight parameters.Rows are sequential coronal slices moving from anterior to posterior. **B,** Second subject. Conventions the same as in **A**.

fractional volume as a function of polar angle separately for the left (blue) and right (red) hemispheres separately, using 16 22.5˚ radial segments. The solid lines represent the mean fractional volume and the shaded region

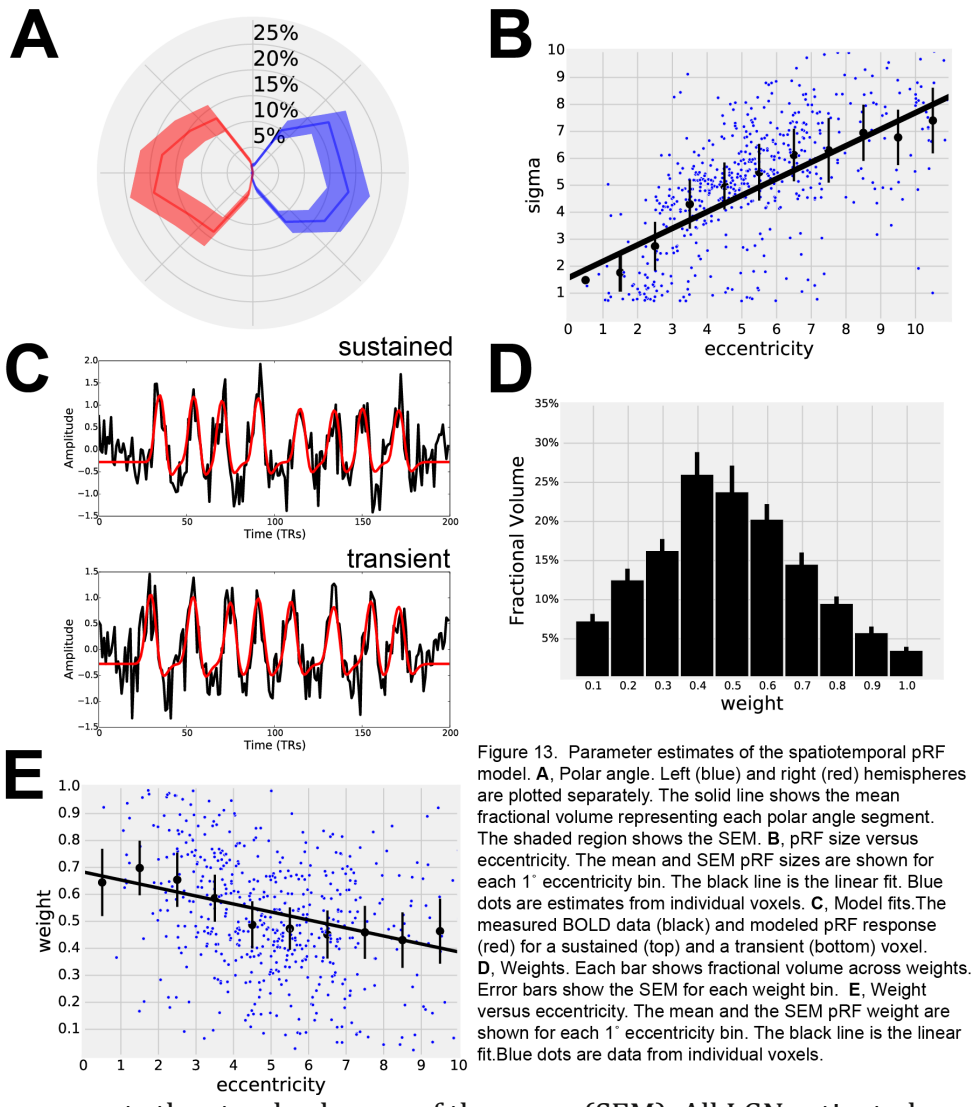

Figure 13. Parameter estimates of the spatiotemporal pRF model. **A**, Polar angle. Left (blue) and right (red) hemispheres are plotted separately. The solid line shows the mean fractional volume representing each polar angle segment. The shaded region shows the SEM. **B**, pRF size versus eccentricity. The mean and SEM pRF sizes are shown for each 1˚ eccentricity bin. The black line is the linear fit. Blue dots are estimates from individual voxels. **C**, Model fits.The measured BOLD data (black) and modeled pRF response (red) for a sustained (top) and a transient (bottom) voxel. **D**, Weights. Each bar shows fractional volume across weights. Error bars show the SEM for each weight bin. **E**, Weight versus eccentricity. The mean and the SEM pRF weight are shown for each 1˚ eccentricity bin. The black line is the linear fit.Blue dots are data from individual voxels.

represents the standard error of the mean (SEM). All LGN activated bilaterally and showed strong contralateral representation of the visual space. In addition, the LGN showed a representational bias such that the horizontal meridians were over-represented and the vertical meridians were under-represented. This representational bias of the retinotopic organization has been shown previously in the LGN and in a number of other visual

subcortical nuclei (Schneider et al., 2004; Schneider and Kastner, 2005, 2009; Schneider, 2011). The eccentricity maps among our subjects showed a similar consistency among subjects and hemispheres, and with our previous reported spatial pRF model estimates in the human LGN. Namely, I found that foveal representations near the posterior pole of the LGN and peripheral representations near the anterior pole of the LGN, with a smooth gradation of eccentricity representations along the anterior-posterior anatomical gradient. Likewise, the pRF size maps showed a similar anterior-posterior gradient with small receptive fields near the fovea and large receptive fields in the periphery. Figure 13B shows the relationship between eccentricity and receptive field size. Here, I plot the spatiotemporal model parameter σ as a function of eccentricity, showing the mean (black dots) and SEM (black bars) binned into 10 1˚ concentric segments. In addition, I show the raw data for all voxels (blue dots) and the linear fit (black line) through all points.

I also found orderly maps of the amplitude and weight parameters. The amplitude maps represent the multiplicative scaling factor used to approximate the unit scale of the measured BOLD response. I found that the amplitude maps were consistent across subjects and hemispheres such that the voxels with the largest amplitudes were clustered near the blood vessel running along the medial-inferior aspect of each LGN, and that the amplitude

decreased towards the lateral-superior aspect of each LGN (Figure 12). The weight maps also showed consistency across subjects and hemispheres. Specifically, I found higher weights along the lateral aspect of the LGN and lower weights along the medial aspect of the LGN (recall that weight of 0 is a purely transient temporal RF response while a weight of 1 is a purely sustained temporal RF response). Figure 13C shows the time-course of two voxels showing the measured BOLD response and the modeled pRF response. The top panel of Figure 13C shows the measured BOLD response (black) and the modeled pRF response (red) for voxels with sustained-rich ($\omega = 0.83$, top) and transient-rich ($\omega = 0.17$, bottom) mixtures. The first four peaks represent the measured (black) and modeled (red) responses to the first set of bar sweeps flickering at 10 Hz. The second set of four peaks represent the measured and modeled responses to the second set of bar sweeps flickering at 20 Hz. The ω parameter of the spatiotemporal pRF model captures the flicker-mediated amplitude modulation such that voxels with a large ω show large amplitude attenuation for the 20 Hz versus the 10 Hz visual flicker stimulation, while voxels with a small ω do not show this attenuation across flicker conditions. Figures 13D and 13E illustrate the distribution of weights among our three subjects and the relationship between weight and eccentricity. I found a negative relationship between the

transient-sustained weight parameter and eccentricity, such that voxels near the fovea tend to have sustained weight estimates while voxels in the periphery tend to have transient weight estimates. Furthermore, I found a negative relationship between the transient-sustained weight parameter and receptive field size, such that voxels with small receptive fields tend to have sustained weight estimates while voxels with large receptive fields tend to have transient weight estimates. Taken together, these results are congruent with previous work showing that parvocellular neurons have small and foveal receptive fields and sustained discharge patterns while magnocellular neurons have large peripheral receptive fields and transient discharge patterns.

Chapter 5: Model-free Functional Segmentation of the LGN

Methods

I have shown that the spatial and temporal tuning properties of the human LGN can be simultaneously estimated using the pRF modeling approach. I have derived retinotopically organized pRF parameter estimate maps in the LGN that are consistent with previous functional imaging work. Furthermore, I have shown that weight parameter estimates of the spatiotemporal pRF model suggest that our stimulus and analysis is able to extract the laminar magnocellular and parvocellular organization of the LGN on the basis of the differential BOLD response to a flickering visual stimulus. In this section, I will lay out two follow-up experiments I conducted in order to corroborate the M/P organization derived using the pRF model. Here, I use a model-free approach to label the voxels of the LGN on the basis of their differential responses to a battery of stimulus features while removing the spatial component from the stimuli.

Display Hardware

The stimuli were generated on a Mac Pro i7 computer (Apple Inc., Cupertino, CA) with a NVIDIA Quadro 4000 video card, using Matlab software (The Mathworks, Natick, MA) and Psychophysics Toolbox 3 functions (Brainard, 1997; Pelli, 1997). Stimuli were presented using a VPixx ProPIXX DLP LED projector (Saint-Bruno, QC, Canada) located outside the scanner room and projected through a wave-guide and onto a translucent screen located at the end of the scanner bore. Subjects viewed the screen at a total viewing distance of 31 cm through a mirror attached to the head-coil. The display subtended approximately 26˚ of visual angle horizontally and 20˚ vertically. In the previous experiment, we ran the projector at a resolution of 960 × 540 and a refresh rate of 480 Hz. For the following experiments, we ran the projector at a resolution of 960 × 540 achromatically at a refresh rate of 1440 Hz (120 Hz × 4 spatial quadrants × 3 color channels). This very high refresh rate increased the gamut of displayable flicker frequencies. As in the previous two experiments, a trigger pulse from the scanner, which was translated into a key press by the response box, was used to synchronize the start of the stimulus.

Visual Stimuli and Procedure

Each subject participated in two follow experiments. The stimulus for the second experiment consisted a checkerboard texture spanning the entire extent of the display (Figure 14A). The luminance of the elements of the checkerboard was sinusoidally modulated between black and white, and was sampled at a rate of 1440 Hz. This high temporal precision in the refresh rate of the display allowed for wider selection of flicker frequencies and finer graduation of the sinusoidal luminance modulation. The scanning run was structured into trials of variable durations and flicker rates. Trial durations and flicker frequencies were sampled from uniform distributions spanning 4 to 6 seconds and 2 to 60 Hz. Each run contained 75 of these trials and lasted approximately 5.5 minutes while subjects fixated a central dot. The same trial structure was used across all scanning runs so that data could be combined across runs and sessions for a given subject.

The stimulus for the third experiment also consisted of a full-field stimulus (Figure 14B), but here we varied the spatial frequency and relative luminance of the elements of a red-green checkerboard texture. The texture subtended the entire display and reversed contrast at 15 Hz. At the outset of each scanning session we used a flicker photometry procedure to determine

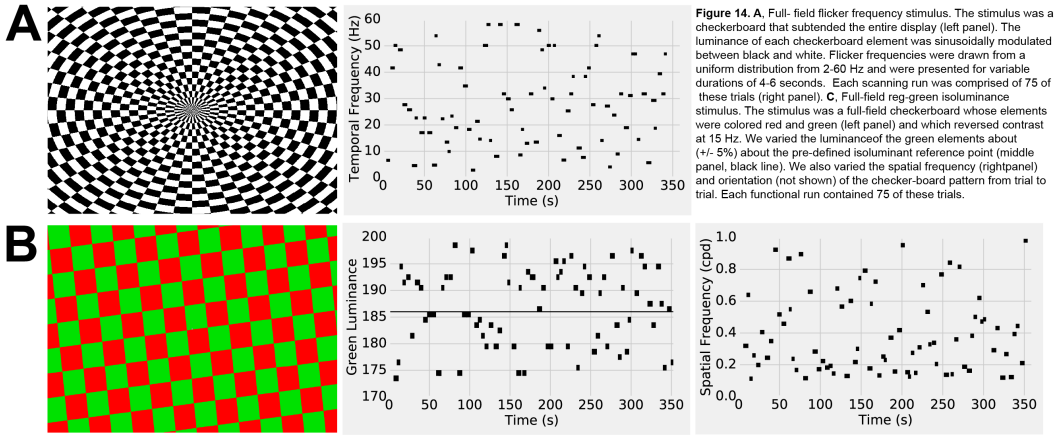

Figure 14. A, Full- field flicker frequency stimulus. The stimulus was a checkerboard that subtended the entire display (left panel). The luminance of each checkerboard element was sinusoidally modulated between black and white. Flicker frequencies were drawn from a uniform distribution from 2-60 Hz and were presented for variable durations of 4-6 seconds. Each scanning run was comprised of 75 of these trials (right panel). **C**, Full-field reg-green isoluminance stimulus. The stimulus was a full-field checkerboard whose elements were colored red and green (left panel) and which reversed contrast at 15 Hz. We varied the luminanceof the green elements about (+/- 5%) about the pre-defined isoluminant reference point (middle panel, black line). We also varied the spatial frequency (rightpanel) and orientation (not shown) of the checker-board pattern from trial to trial. Each functional run contained 75 of these trials.

each subject's isoluminance for red-green. Subjects were presented with a red-green checkerboard texture that reversed contrast at 15 Hz. Their task was to adjust the green luminance in order to minimize the heterochromatic flicker (Tansley and Boyton, 1976), and we took the mean of 30 such calibration trials to constitute an isoluminant reference point. From trial to trial, we varied the spatial frequency and divergence from the isoluminant reference point (Figure 14B, black line). Spatial frequencies were uniformly sampled from 0.1 to 1 cycles-per-degree (cpd) in log-space, and the green luminance was varied 5% above and below the empirically determined isoluminant reference point. Each run contained 75 of these trials and lasted approximately 6 minutes while subjects fixated a central dot.

Model-free Functional Segmentation of the LGN

The spatiotemporal pRF model parameter ω provides a measure of the relative contribution of the aggregate magnocellular and parvocellular responses contained within a single voxel and encoded in the BOLD response. The parameter estimate varies between 0 and 1, with 0 being a purely transient response and 1 being a purely sustained response. The distribution of the ω parameter estimates across the LGN, then, represents a functional gradient rather than a functional segmentation per se. In order to determine if the distribution of ω estimates across the LGN emanates from the magnocellular and parvocellular response properties, we designed full-field stimuli that varied stimulus properties over time so as to maximally differentiate the presumptive signal of the M and P layers. Voxels containing a preponderance of magnocellular or parvocellular neurons should show a unique pattern of BOLD activation depending on the flicker frequency, the spatial frequency, and departures from red-green isoluminant reference point. We used two model-free approaches to classify voxels on the basis of the BOLD response to the full-field stimuli. Only voxels that survived an activation threshold ($r^2 > .10$), computed by regressing the measured BOLD response against the modeled pRF response) from experiment 1 were used.

The BOLD time-series of the surviving voxels from the two full-field experiments were concatenated in time and a dissimilarity matrix was computed by taking the pairwise Euclidean distance of the estimated covariance matrix. This dissimilarity matrix was then clustered using an agglomerative hierarchical clustering algorithm (Pedregosa et al., 2011), specifying a cluster size of two. In addition to clustering, we also performed an independents components analysis (ICA) decomposition (Pedregosa et al., 2011) specifying 20 components. Thus, each voxel contained 6 spatiotemporal pRF model parameter estimates ($x, y, \sigma, \omega, \beta, \mu$), a cluster label (1 or 2), and 20 z-scored ICA component loadings. We used a stepwise regression to determine the relationship between the 6 spatiotemporal pRF model estimates and cluster labels across the three subjects' LGN. This procedure allowed to rank order the pRF parameter estimates according to how well they predict the clustering labels. In addition, I used an ordinary least squares (OLS) regression of the ICA components against the pRF estimates to identify ICA components of interest. We also regressed the ICA components against the sum of the pRF estimates in order to identify components that are not well explained by any of our pRF model parameter estimates.

Results

The weight parameter of the spatiotemporal pRF model provides a continuous measure of the relative contribution of the parvocellular and magnocellular neural subpopulations towards the aggregate BOLD signal. Since it is exceedingly unlikely that any given voxel would sample from a purely parvocellular or magnocellular neural population, the weight parameter represents a functional gradient rather than a functional clustering. Voxels may have a weight estimate indicative of a parvocellular population with a sustained discharge pattern or a magnocellular population with a transient discharge pattern. However, since we have no clear *a priori* threshold for binarizing our weight map into an M/P map, we sought to independently segment the LGN on the basis of the functional activity in response to a number of relevant stimulus features. We presented subjects with full-field stimuli in order to remove any spatial component from the BOLD signal and varied the stimulus properties to maximally differentiate the presumptive magnocellular and parvocellular responses underlying the BOLD signal. Figure 15 shows detailed maps of the results of a hierarchical clustering analysis (column 1) and ICA decomposition (columns 2-8) for two

subjects (panels A and B) that were performed on the full-field flicker

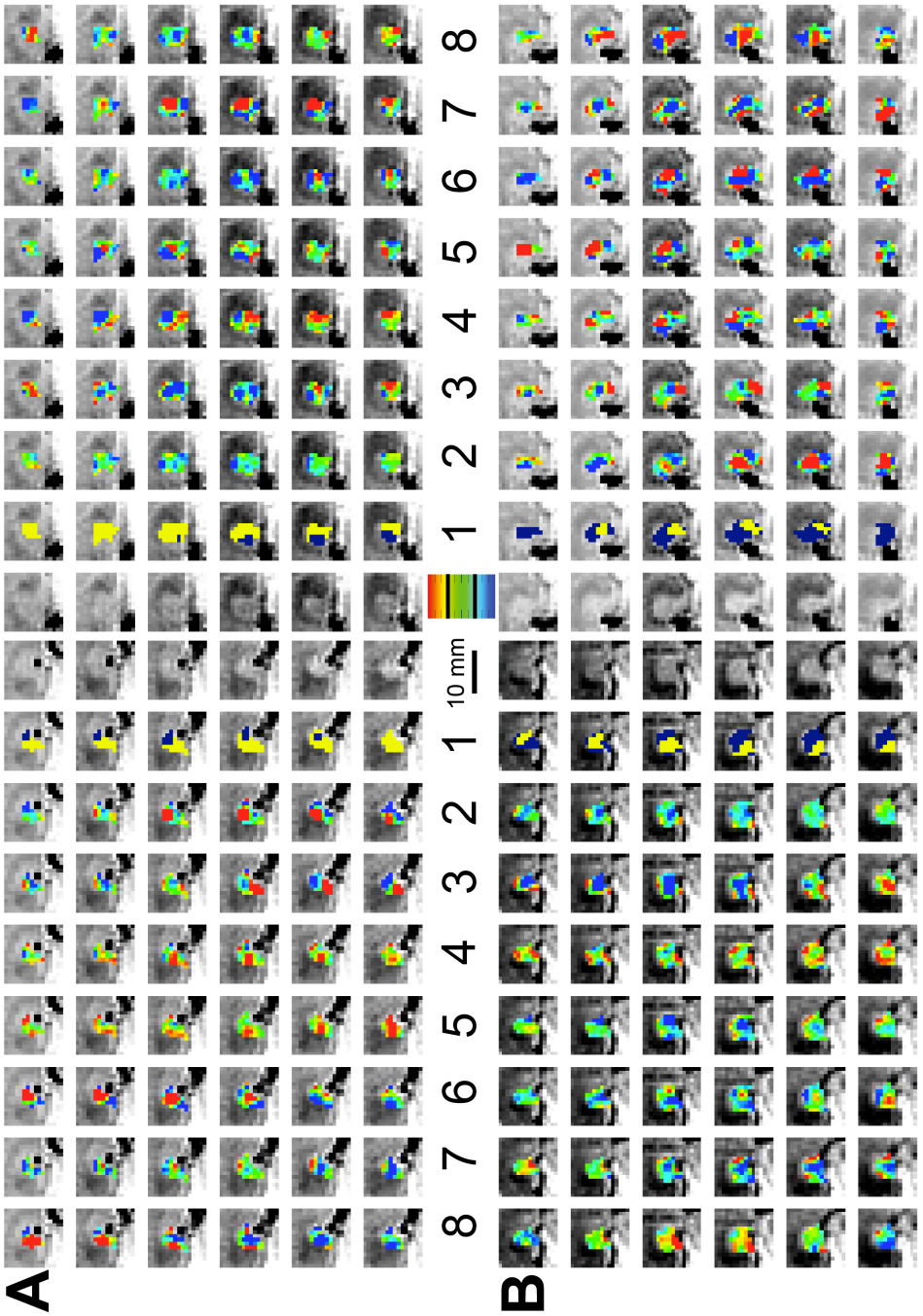

Figure 15. Detailed model-free measurement maps in the human LGN. **A**, Parameter estimates overlaid atop the PD image for both the left and right LGN for a single subject. The innermost columns show the unlabeled PD image followed by the cluster labeling (1). The rest of the columns show the ICA components that correlated best with cluster labels (2), polar angle (3), eccentricity (4), receptive field size (5), weight (6), and amplitude (7) parameter estimates from the pRF model. The outermost column shows the component which covaried the least with the sum of all the pRF model parameter estimates (8). Rows are sequential coronal slices moving from anterior to posterior. **B**, Second subject. Conventions the same as in **A**. All ICA component loadings were z-scored. The color legend is in the center of the figure, and the black ticks at the top and bottom of the colorbar indicate z = 0.8 and z = -0.8, respectively.

frequency and isoluminance functional data concatenated in time. As in Figure 12, we present the measures overlaid atop consecutive coronal slices of the PD image, and we show the unlabeled anatomical slices in the innermost column of panels A and B. Column 1 shows the cluster labels that were extracted from the functional data collected while subjects viewed the full-field stimuli. For all three subjects, we found consistent spatial clustering such that the classification subdivided the left and right LGN along a medial-lateral axis with common cluster labels among voxels along the lateral extent of the left and right LGN and common cluster labels among voxels along the medial extent of the left and right LGN. We performed a stepwise regression in order to determine which of the pRF model parameter best predict the cluster labels (Table 2). A stepwise regression iteratively modifies a linear model through the inclusion/exclusion of model factors in the pursuit of maximizing the explained variance. We found that cluster labeling was best explained by a model that included only the weight and amplitude parameter estimates [$F(2,636) = 45.43$, $p < .0001$, $r^2 = .125$]. Furthermore, while the weight ($beta$ = -.31, $t(638) = -4.50$, $p < .0001$) and amplitude ($beta$ = .21, $t(638) = 9.39$, $p < .0001$) were both predictive for the voxel-wise hierarchical cluster labeling, the coefficient associated with these parameters were

oppositely signed suggesting that these factors each explain separable variance components in the data.

In addition to clustering, we also performed an ICA decomposition of each subject's full-field functional data, specifying 20 components. This analysis was considered exploratory, in that the aim was to evaluate how much information our pRF model can account for in the functional data driven by the full-field stimuli. Columns 2 through 8 of Figure 5 show the z-scored loadings for components that we identified as components of interest based on the results of an OLS regression. We regressed the 20 ICA components against each of the pRF model parameter estimates. Columns 3 through 7 show the components that significantly ($p < .0001$) covaried with and best explained the polar angle (3), eccentricity (4), receptive field size (5), sustained-transient weight (6), and amplitude (7) parameter estimates. The components in columns 4, 5, and 6 all showed a similar pattern of

pRF parameter	β	SE	p-value
polar angle	.0064	.0092	.4870
eccentricity	-.0026	.0064	.6801
receptive field size	-.0039	.0065	.5490
weight	-.3091	.0687	< .0001
amplitude	.2091	.0223	< .0001
baseline	.3195	.4129	.4349

Table 3. Summary of the stepwise regression, $r^2 = .125$.

activation with a large positive loading oriented towards the lateral portion of the LGN and a large negative loading oriented towards the medial portion of the LGN. This suggests that there exists an underlying topographical organization that is common among these three model parameters: namely, that voxels with small foveal receptive field and a sustained-rich weight covary with one another and are functionally complementary to voxels with large peripheral receptive fields and a transient-rich weight. Column 2 of Figure 5 shows the loadings for the component that best explains the cluster labeling derived from each subject's full-field functional dataset. These results suggest that our pRF model estimates can, in part, explain some of the variance we found in our full-field experiments. To test this further, we also regressed the 20 ICA components against the sum of the pRF model parameter estimates in an effort to find a component that could not explain the variance we see in our parameter maps. We take the sum of the pRF model parameters to represent the variation captured by the model as a whole. Column 8 of Figure 5 shows the loadings for the component that does *not* significantly covary with the sum of estimates and so constitutes variance in the full-field data that is not captured by any of our pRF model parameters. That the loading maps for these components in each of subjects' LGN shows a certain degree of structure and spatial correlation further suggests that there

are sources of variance in the LGN which are not explained by our spatiotemporal pRF model.

Chapter 6: Discussion

Spatial pRF Estimation Across Subcortex

Here, I have demonstrated that the pRF model can be used to estimate the spatial tuning properties of multiple subcortical nuclei. I was able to verify the retinotopic organization of the LGN and SC as described previously both in the electrophysiology (Moschovakis et al., 1996; Sparks, 1986, 2002; Wurtz and Albano, 1980; Goldberg and Wurtz, 1972; Berman and Cyander, 1972) and functional imaging (Schneider et al., 2004; Schneider et al., 2005; Schneider and Kastner, 2005; Schneider and Kastner, 2009; Katyal et al., 2010; Schneider, 2011) literature. The pRF sizes I measured in the LGN were roughly equivalent to the neural RF sizes in the macaque for parafoveal locations; however, at eccentricities of 10° and greater, our measured pRF sizes were approximately double that of previous reports using neurophysiological techniques (Xu et al., 2001; Xu et al., 2002). The pRF sizes I found in the SC were in agreement with the neural RF sizes measured in the cat (Berman and Cyander, 1972).

None of these previous subcortical retinotopic mapping studies made use of the PD images for defining the anatomical boundaries of the LGN or of

other subcortical nuclei. Defining the LGN based on functional activation (Schneider et al., 2004) resulted in volumes roughly double those reported in the post-mortem human (Andrews et al., 1997). This overestimation of the anatomical boundaries of the LGN, based on functional activation, most likely emanates from the inclusion of similarly entrained voxels sampling from nearby blood vessels and subcortical nuclei such as the triangular area, pulvinar nuclei, and the TRN. Such an approach will lead to inaccuracies in determining the properties of the LGN, especially when attempting to measure variations throughout the structure of the LGN as might be expected from its anatomical subdivisions (Schneider et al., 2004; Denison et al., 2014; Zhang et al., 2015).

I also found orderly retinotopic organization in the SC using the spatial pRF model. Neurons in the superficial layers of the SC respond well to a variety of visual stimuli regardless of contrast, orientation, size, shape, or velocity (Humphrey, 1968; Schiller and Koerner, 1971; Cynader and Berman, 1972; Goldberg and Wurtz, 1972; Schiller and Stryker, 1972; Marrocco and Li, 1977). Moreover, the activity of the SC is highly modulated by spatial attention and by task-related attentional switching between the motion and color features of a visual stimulus (Schneider, 2011). This study also found that the activity of the SC did not modulate with feature-based attention.

Taken together, these results suggest that the SC plays a role in representing behaviorally relevant visual stimuli in terms of the retinotopic space, and that signals from the SC may provide a mechanism for anticipatory and orienting behaviors.

In addition to the LGN and SC, I discovered a number of subcortical nuclei, across all three subjects that showed an orderly retinotopic organization. Surprisingly, I found contralateral hemifield representations in the pars reticulata of the SN. In the macaque, the pars reticulata of the SN receives direct projections from the striatum and possibly indirect projections through the caudate nucleus from the frontal eye fields and the thalamus (Hikosaka and Wurtz, 1983a). Neurons of the pars reticulata in turn project onto the intermediate and deep layers of the SC (Hikosaka and Wurtz, 1983a; Hikosaka and Wurtz, 1983d). Neurons in the pars reticulata are retinotopically organized and discharge in response to the presentation of visual stimuli (Hikosaka and Wurtz, 1983a; Hikosaka and Wurtz, 1983b). Responses are also evoked during visually- and memory-guided saccadic eye movements (Hikosaka and Wurtz, 1983c; Hikosaka and Wurtz, 1983d). Furthermore, antidromic activation from the SC showed that the RFs of neurons in the pars reticulata of the SN the movement fields of neurons in the intermediate layers of the SC were visuotopically aligned (Hikosaka and

Wurtz, 1983d). These response characteristics, along with evidence for the interconnectivity of the pars reticulata with the striatum and the superior colliculus, suggest that the pars reticulata is critical for representing the spatial location of a saccadic target and may even play a role in the initiation of the saccade itself (Hikosaka and Wurtz, 1983d). While the encoding stimulus in this study included an attention task at fixation, it is possible that the sweeping bar stimulus constituted a highly salient visual stimulus that the SN represented as a potential target for a saccade. The signal in the pars reticulata signal could, in turn, project to the SC for the purpose of orienting attention and behavior. Degeneration of the pars reticulata of the SN has been associated with Parkinson's disease (Tseng et al., 2000) and epilepsy (Deransart et al., 2003). The pRF model as described here may offer an avenue for determining the functional viability of the SN and should be considered by researchers investigating these pathologies.

I also found a retinotopic map in the TRN. The TRN is a thin layer of γ-Aminobutyric acid (GABA) releasing cells abutting the dorsolateral and anterior segments of the thalamus (Jones, 1975). The TRN receives topographic inputs, and drives inhibitory feedback, to thalamic relay cells via GABA receptors (Kim et al., 1997, and is known to contain visually-responsive regions (Montero et al., 1977; Pinault et al., 1995; Wang et al.,

2001). The TRN has been shown to have topographically preserved reciprocal connections with both the LGN (Harting et al., 1991) and visual cortex (Sherman and Guillery, 1996). The TRN is thought to play a role in visual spatial attention through the coordination of activity in the LGN and pulvinar, and might be a candidate for the seat of the "attentional spotlight" in the early visual system (Crick, 1984). This suggests that adding a spatial attention component to the encoding stimulus may aid in retinotopically mapping the TRN and other thalamic nuclei with which the TRN has an antagonistic relationship. The encoding stimulus in this study included an attention task at fixation, which may have resulted in a non-spatially specific amplification of the BOLD signal in the TRN. A recent functional imaging study of the human TRN showed that bilateral TRN activation can be measured by modulating visual flicker (Viviano and Schneider, 2015). Likewise, I found the polar angle representation of the TRN to be more ipsilateral than in any of the other subcortical nuclei. The TRN also differed from the other nuclei in that the distribution of HRF delays across the TRN was relatively uniform whereas other structures followed a more Gaussian distribution. The pRF sizes in the TRN were found to be roughly equivalent to those reported in the macaque at the eccentricities stimulated (McAlonan et al., 2006).

The retinotopic organization of the pulvinar has been reported previously in nonhuman and simian primate species using single-cell recordings (Bender, 1981; Li et al., 2013), demonstrating two separate retinotopic representations of the visual field. Using the pRF model, I identified two separate retinotopic maps in the human pulvinar, which I have determined to be the LP and the IP based on an anatomical atlas (Mai et al., 2008). The LP and IP have a similar polar angle representation where the upper vertical meridian is represented more inferiorly and laterally while the lower vertical meridian is represented more superiorly and medially. The orientations of our pRF maps correspond well with previous imaging experiments in the human pulvinar (Cotton and Smith, 2007; Smith et al., 2009; Schneider, 2011). I also found that the IP shares a foveal representation with the LP, and a positive relationship between pRF size and eccentricity. The pulvinar is the largest nucleus in the primate thalamus, and is highly spatially selective (Schneider, 2011). Neurons in the pulvinar encode a number of visual features direction of motion and orientation (Mathers and Rapisardi, 1973; Gattass et al., 1979; Benevento and Miller, 1981; Casanova et al., 2001), and the activity of these neurons is modulated by spatial attention (LaBerge and Buchsbaum, 1990; Bender and Youakim, 2001; Kastner et al., 2004; Schneider and Kastner, 2009). In non-human

primates, it has been shown that the pulvinar provides indirect connectivity between cortical areas that are themselves directly connected, and these connections from visual cortical areas target portions of the pulvinar in a topographic manner (Benevento and Rezak, 1976; Ungerleider et al., 1984). Recent neuroimaging studies of the human pulvinar has shown that the general organization is very similar to that found in the nonhuman primate pulvinar (Arcaro et al., 2015). Using a phase-encoding approach, these researchers found evidence for four separate retinotopic maps in the human pulvinar. The location and orientation of the maps in the inferior and lateral pulvinar are in agreement with the maps we found in IP and LP using the spatial pRF model.

Among all the subcortical nuclei, I found a consistent under-representation of the vertical meridians and an overrepresentation of the horizontal meridians. This bias has been previously reported in the LGN, the SC, the IP, and the LP (Schneider et al., 2004; Schneider et al., 2005; Schneider and Kastner, 2009; Schneider, 2011). This is unlikely to be due to partial volume effects, as previous work in our lab has shown that the vertical meridians, located at the edges of the LGN, could not be recovered by dilating the LGN mask to also include a one-voxel shell around the functionally defined ROI (Schneider et al., 2004). Furthermore, I am

confident that I sampled the entire LGN volume in the present study since the ROI were defined using a PD weighted image independent of the functional data.

In addition to deriving the spatial tuning of each voxel, I also estimated the voxel-wise HRF delay. Since each bar sweep traversing the display was paired with a sweep in the opposite direction, the spatial tuning parameters were not degenerate with the HRF delays, and I was able to estimate the delay of the peak and undershoot of the HRF for each voxel. I estimated the delay of the peak and undershoot per voxel concomitantly with the spatial tuning parameters. Other approaches have estimated the voxel-wise HRF using an independent dataset (Dumoulin and Wandell, 2008) or an iterative fitting procedure where the spatial tuning is first derived using the canonical double-gamma HRF (Friston et al., 1998; Glover, 1999; Worsley et al., 2002) after which the HRF is modeled from a fixed spatial tuning estimate (Harvey and Dumoulin, 2011). The advantages of estimating the HRF delay are two fold. First, estimating the HRF delay may help offset inter-regional and inter-subject variability in hemodynamics that could obfuscate the spatial tuning among voxels in various subcortical nuclei (Handwerker et al., 2004). Second, the HRF delay estimate may offer insight into the network dynamics in the visual system. For instance, I measured the HRF delay in the

SC to be about one acquisition volume shorter than that found in the other five subcortical nuclei. High-field imaging in the rat during brief visual presentation has also shown that the time-to-peak in the SC is earlier than in the LGN (Lau et al., 2011). Accounting for differences in the HRF among subcortical nuclei may be critical for estimating their other functional properties, such as spatial tuning or the flow the information through the visual system. Neurons in the macaque SC have been shown to discriminate stimulus features prior to the initiation of a saccade and with very short latencies (Horowitz and Newsome, 1999), suggesting that the SC maintains an early representation for visual stimuli. Our HRF delay estimates in the SC lend further support to the dual pathway model of visual processing, where information flows from retina to cortex both through a geniculo-striate and an early collicular-pulvinar route (Berman and Wurtz, 2010; Berman and Wurtz, 2011).

The relationship between eccentricity and pRF size in the subcortex closely resembles that found in cortex (Dumoulin and Wandell, 2008)—however, the pRF sizes measured in the LGN are somewhat larger than what has been reported previously in subcortex using electrophysiology techniques (Xu et al., 2001; Xu et al., 2002). There are at least three possible sources of pRF size misestimation that may be particular to subcortex. First,

due to the deep anatomical location of the subcortical nuclei, the BOLD signal in these brain areas has a relatively low signal-to-noise ratio. In order to maximize the signal strength, the duty-cycle of the sweeping bar stimulus was set to one-half. This ensures that any given location in the visual field is stimulated for approximately half the duration of a given bar sweep and of a scanning run. And while this has the effect of making the most of scanner time, it may also have the effect of diminishing the precision of the pRF model in estimating the pRF size. Ideally, the stimulation run should vary the width of the sweeping bar in order to optimize the relationship between BOLD signal saturation and duty cycle for better estimation of the receptive field size. Second, since these subcortical nuclei are small compared to their cortical counterparts, the entirety of the contralateral hemifield is represented in a relatively small amount of tissue, resulting in a steep local visuotopic gradient per MRI voxel. I estimated the local retinotopic gradient and deconvolved it from the pRF size, finding that the measured pRF size approximates the simulated neural RF size well, and that the local visuotopic gradient plays a small role in inflating the pRF size. Third, the point-spread function of the BOLD signal at 3T has been estimated to be 3–4 mm FWHM (Parkes et al., 2005). In cortex this approximates the voxel size, but in

subcortex where smaller voxels are used it introduces a sizeable and implicit spatial smoothing factor that could inflate the pRF size.

Spatiotemporal pRF Model

The pRF model has been used to explore and describe the visual responses measured in a number of subcortical and cortical areas (Dumoulin and Wandell, 2008; Amano et al., 2009; Harvey et al., 2013, Kay et. al, 2013) using functional imaging techniques. Since its inception, it has proved to be a robust and expressive model for capturing and formulating the tuning properties throughout the visual pathway. Within the sphere of retinotopic mapping, the Gaussian pRF model has supplanted the phase-encoding mapping approach (Engel et al., 1994; Sereno et al., 1995), in part owing to the fact that estimation of the pRF model is driven by an effective stimulus that can encode multiple features in parallel. The pRF model has also been extended to the auditory domain to map the tonotopic organization of the human auditory cortex (Thomas et al., 2015). I sought to extend the pRF model into the temporal domain in an effort to explore the response properties of the human LGN, and to segment it on the basis of its function.

I have developed a spatiotemporal pRF model that includes both spatial and temporal receptive fields to capture differences in the response properties of neurons in the magnocellular and parvocellular layers of the LGN. While difficult to measure because of its small size and deep location in the brain, the unique functional and structural organization of the LGN offers a rich experimental arena in which to develop and test models of information flow and dysfunction throughout the visual system. Among their distinguishing characteristics, the M and P layers of the LGN are dissociable based on their response profiles to various stimuli. In particular, I sought to exploit the differences in the temporal frequency tuning and discharge patterns among magnocellular and parvocellular neurons. I extended the spatial pRF model to include a pair of temporal receptive fields, where the ideal parvocellular response was modeled as a Gaussian in time and the magnocellular response was modeled its first derivative. The aggregate BOLD response was taken to be the weighted sum of the transient and sustained responses, in combination with the spatial and hemodynamic components. The functional form of the temporal RF helps to link the neural response properties of temporal frequency tuning and the discharge pattern. A transient discharge pattern—the rapid cycling of neural activity—acts as an edge detector in time and so confers the property of high temporal

frequency tuning. A sustained discharge pattern—tonic activation during the presentation of a stimulus—acts as a low-pass temporal filter and confers the property of low temporal frequency tuning. When a stimulus with varied flicker frequencies is passed through the temporal RFs, the resulting response will demonstrate a frequency-driven amplitude modulation over time. Thus, the spatiotemporal pRF model estimation affords information about how a given voxel is tuned in space and time.

The retinotopic organization of our LGN maps is consistent with our previous work. All LGN showed strong contralateral representation of the visual field, with the lower vertical meridian representation along the superior-medial LGN, the upper vertical meridian representation along the inferior-lateral LGN, and the contralateral horizontal meridian bisecting the two about approximately 45˚. The eccentricity and receptive field size maps showed a strong positive relationship such that voxels at the posterior pole of the LGN had small, foveal receptive fields and voxels at the anterior pole of the LGN had large, peripheral receptive fields. These findings demonstrate that the spatial component of the spatiotemporal model can be faithfully estimated with a stimulus that encodes multiple features.

In addition to the spatial tuning, I was also able to recover the topographic organization of the temporal tuning across the LGN. Among our

three subjects, I found a smooth gradation of the weight parameter estimates along the lateral-superior to medial-inferior axis of the LGN. Specifically, I found that voxels along the lateral-superior portion of the LGN contained voxels with sustained-rich weight estimates and voxels along the medial-inferior portion of the LGN contained voxels with transient-rich weight estimates. The configuration and orientation of these weight parameter maps is congruent with the known structural and functional organization of the LGN. Previous functional imaging experiments aimed at dissociating the M and P layers of the human LGN have found a similar organization of the regression coefficients computed from a GLM using a battery of M-preferred and P-preferred stimuli (Denison et al., 2014; Zhang et al., 2015) including spatial frequency, temporal frequency, color, and contrast. The experiments relied on the centers of mass of the beta weights associated with M-preferred and P-preferred stimuli to determine the anatomical axis of the functional topography. I find these approaches problematic for several reasons. First, LGN ROI were determined on the basis of the functional activation. Since the LGN is flanked by several visually responsive structures including the triangular area, the pulvinar, and blood vessel, functional definition of the LGN will invariably result in the inclusion neighboring voxels not belonging to the LGN. In the present study, each subject participated in an anatomical

scanning session where 40 proton-density weighted images were collected, registered, and averaged. These data provided a clear anatomical image for determining the location and extent of the LGN without relying on functional measures. Second, the regression coefficients that form the basis of the functional topography offered in previous studies share only a statistical relationship with the stimuli that drove the activity. In the present study, I used a modified version of the pRF model in order to obtain estimates of the topography of the LGN. Since the pRF model parameters are stimulus-referred, the topography of the LGN can be expressed specifically in terms of spatial and temporal tuning. The pRF model also provides the opportunity to make specific predictions the stimulus-contingent BOLD response where the GLM cannot. Both our weight estimate maps and the previously reported beta coefficient maps (Denison et al., 2014; Zhang et al., 2015) have a similar orientation and configuration in the LGN, whereby functional topography shows a gradation along the superior-lateral to inferior-medial LGN. In addition to our weight estimate maps, I also find that the amplitude estimate maps have a very similar topography to the GLM beta coefficient maps reported previously. It may be that these previously reported M/P maps are extracting information about the gain of the BOLD response as a function of distance from the vasculature since their regression coefficient maps and our

amplitude maps show greatest amplitudes near the vessel and a graduated amplitude decrease for voxels farther away from the vessel adjacent to the medial surface of the LGN.

Model-free Functional Segmentation of the LGN

In order to determine how much of the variation in the activity of the LGN the spatiotemporal pRF model captures, we decided to perform two follow up experiments. Here, we removed any spatial component from the stimulus and presented subjects with full-field checkerboard stimuli whose flicker frequency, spatial frequency, and red-green isoluminance were varied so as to maximally differentiate the underlying M and P response in the LGN. We then used model-free clustering and decomposition techniques in order to determine if we could replicate the topographies of the pRF model parameter estimate maps in Chapter 4. The results of our hierarchical clustering revealed a topographic organization of the cluster labeling that agreed with our weight estimate maps. Specifically, we found two classes of spatially correlated voxels in each subject that were organized along a medial-to-lateral axis. A stepwise regression showed that the weight and amplitude parameter estimate maps best explained the clustering we derived among

our three subjects. We also found that in all subjects we could find ICA components whose loadings significantly covaried with each of the parameter estimates derived from the pRF model, suggesting that even in the absence of a spatial signal the intrinsic connectivity of the LGN can be extracted from the retinotopic organization. We also found components that did not significantly covary with the sum of the pRF estimate maps, suggesting that there exists some variability in the activity of the LGN that remains unexplained by the pRF model.

The model-free functional segmentation experiment was developed with the intention of aiding in the interpretation of the spatiotemporal model estimates. Since the weight parameter of the spatiotemporal pRF model expresses the relative contribution of parvocellular and magnocellular neural populations on the measured BOLD response and because we have no *a priori* threshold for determining the M/P membership of a given voxel based on its weight estimate. Moreover, Maunsell and colleagues (1999) showed that in response to a light stimulus, magnocellular and parvocellular neurons both showed strong transient discharge patterns, while only parvocellular neurons showed a persistent and sustained discharge throughout the stimulus duration. This finding has important consequences for the interpretation of the spatiotemporal pRF model weight parameter estimates.

First, it suggests that one should not expect to find a purely sustained response even if one were able to sample from a voxel containing only parvocellular neurons. Within the specific context of spatiotemporal pRF model, we should not expect to find voxels with a weight estimate approaching 1.0, since the neural responses of parvocellular neurons show both transient and sustained components. On the other hand, we should expect to find many voxels whose weight estimates approach 0. Adopting a somewhat naïve interpretation of the weight parameter, I could consider any weight estimate below 0.5 as magnocellular and any weight estimate above 0.5 as parvocellular. On this assumption and the on basis of anatomical studies of the human LGN, we should expect that 80% of the LGN voxels should have weight estimates above 0.5, since the parvocellular layers makeup approximately 80% of the LGN volume. However, I found that 40% of our activated LGN volumes had weight estimates in the parvocellular range. This might suggest that our model is biased towards transient weight estimates, or it might suggest something about the prevalence of transient discharge patterns in the underlying neural populations.

References

Amano K, Wandell BA, Dumoulin SO. (2009). Visual field maps, population receptive field sizes, and visual field coverage in the human MT+ complex. Journal of Neurophysiology 102:2704-2718.

Andrews TJ, Halpern SD, Purves D. (1997). Correlated size variations in human visual cortex, lateral geniculate nucleus, and optic tract. Journal of Neuroscience 17:2859-2868.

Arcaro MJ, Pinsk MA, Kastner S. (2015) The anatomical and functional organization of the human visual pulvinar. Journal of Neuroscience 35:9848-9871.

Astruc J. (1971). Corticofugal connections of area 8 (frontal eye field) in Macaca mulatta. Brain Research 33:241–256.

Bender DB. (1981). Retinotopic organization of macaque pulvinar. Journal of Neurophysiology 46:672-693.

Bender DB. (1982). Receptive-field properties of neurons in the macaque inferior pulvinar. Journal of Neurophysiology 48:1-17.

Bender YA, Youakim M. (2001) Effect of attentive fixation in macaque thalamus and cortex. Journal of Neurophysiology 85:219-234.

Benevento LA, Miller J. (1981). Visual responses of single neurons in the caudal lateral puvlinar of the macaque monkey. Journal of Neuroscience 1:1268-1278.

Benevento LA, Rezak M. (1976) The cortical projections of the inferior pulvinar and adjacent lateral pulvinar in the rhesus monkey: an autoradiographic study. Brain Research 108:1-24.

Berman N, Cyander M. (1972). Comparison of receptive-field organization of the superior colliculus in siamese and normal cats. Journal of Physiology 224:363-389.

Berman RA, Wurtz RH. (2010). Functional identification of a pulvinar path from superior to cortical area MT. Journal of Neuroscience 30:6342-6354.

Berman RA, Wurtz RH. (2011). Signals conveyed in the pulvinar pathway from superior colliculus to cortical area MT. Journal of Neuroscience 31:373-384.

Brainard DH. (1997). The psychophysics toolbox. Spatial Vision 10:433-436.

Casanova C, Merabet L, Desautels A, Minville K. (2001). Higher-order motion processing in the pulvinar. Progress in Brain Research 134:71-82.

Connolly M, Van Essen D. (1984). The representation of the visual field in the parvocellular and magnocellular layers of the lateral geniculate nucleus in the macaque monkey. Journal of Comparative Neurology 226:544-564.

Cotton PL, Smith AT. (2007). Contralateral visual hemifield representations in the human pulvinar nucleus. Journal of Neurophysiology 98:1600-1609.

Deransart C, Hellwig B, Heupel-Reuter M, Léger J, Heck D, Lücking CH. (2003). Single-unit analysis of substantia nigra pars reticulata neurons in freely behaving rats with genetic absence epilepsy. Epilepsia 44: 1513-1520.

Dumoulin S, Wandell BA. (2008). Population receptive field estimates in human visual cortex. NeuroImage 39:647-660.

Finlay BL, Schiller PH, and Volman SF. (1976). Quantitative studies of single-cell properties in monkey striate cortex. IV. Corticotectal cells. J Neurophysiology 39:1352-1361.

Fries W. (1984). Cortical projections to the superior colliculus in the macaque monkey: a retrograde study using horseradish peroxidase. Journal of Comparative
Neurology 230:55-76.

Fries W, Distel H. (1983). Large layer VI neurons of monkey striate cortex (Meynert cells) project to the superior colliculus. Proceedings of the Royal Society B: 219: 53–59.

Friston KJ, Fletcher P, Josephs O, Holmes A, Rugg MD, Turner R. (1998). Event-related fMRI: characterizing differential responses. NeuroImage 7:30-40.

Gattass R, Oswaldo-Cruz E, Sousa AP. (1979). Visual receptive fields of units in the pulvinar of cebus monkey. Brain Research 160:413-430.

Glover, GH. (1999). Deconvolution of impulse response in event-related BOLD fMRI. Magnetic Resonance in Medicine 42:290-299.

Goldberg ME, Wurtz RH. (1972). Activity of the superior colliculus in behaving monkey, I. visual receptive fields of single neurons. Journal of Neurophysiology 35:542-559.

Graham J. (1982). Some topographical connections of the striate cortex with subcortical structures in Macaca fascicularis. Experimental Brain Research 47:1–14.

Haak KV, Cornelissen FW, Morland AW. (2012). Population receptive field dynamics in human visual cortex. PLoS ONE 7:e37686.

Handwerker DA, Ollinger JM, D'Esposito M (2004) Variation of BOLD hemodynamic responses across subjects and brain regions and their effects on statistical analyses. NeuroImage 21:1639–1651.

Hartin JK, Van Lieshout DP, Feig S. (1991). Connectional studies of the primate lateral geniculate nucleus: distribution of axons arising from the thalamic reticular nuclei. Journal of Comparative Neurology 310:411-427.

Harvey BM, Dumoulin SO. (2011). The relationship between cortical magnification factor and population receptive field size in human visual

cortex: constancies in cortical architecture. Journal of Neuroscience 31:13604-13612.

Hikosaka O, Wurtz RH. (1983a). Visual and oculomotor functions of monkey substantia nigra pars reticulata. I. Relation of visual and auditory responses to saccades. Journal of Neurophysiology 49:1230-1253.

Hikosaka O, Wurtz RH. (1983b). Visual and oculomotor functions of monkey substantia nigra pars reticulata. II. Visual responses related to fixation of gaze . Journal of Neurophysiology 49:1254-1267.

Hikosaka O, Wurtz RH. (1983c). Visual and oculomotor functions of monkey substantia nigra pars reticulata. III. Memory-contingent visual and saccade responses. Journal of Neurophysiology 49:1268-1284.

Hikosaka O, Wurtz RH. (1983d). Visual and oculomotor functions of monkey substantia nigra pars reticulata. III. Relation of substantia nigra to superior colliculus. Journal of Neurophysiology 49:1285-1301.

Horowitz GD, Newsome WT. (1999). Separate signals for target selection and movement specification in the superior colliculus. Science 284:1158-1161.

Humphrey NK. (1968) Responses to visual stimuli of units in the superior colliculus of rats and monkeys. Experimental Neurology 20:312-340.

Jancke D, Erlhagen W, Schoner G, Dinse HR. (2004). Shorter latencies for motion trajectories than for flashes in population responses of cat primary visual cortex. Journal of Physiology 556:971-982.

Jones, EG. (1975). Some aspects of the organization of the thalamic reticular complex. Journal of Comparative Neurology 162:285-308.

Kastner S, O'Connor DH, Fukui MM, Feld HM, Herwig U, Pinsk MA. (2004). Functional imaging of the human lateral geniculate nucleus and pulvinar. Journal of Neurophysiology 91:438-448.

Kim, U, Sanchez-Vives, MV, and McCormick, DA. (1997). Functional dynamics of GABAergic inhibition in the thalamus. Science 278:130–134.

Krauzlis RJ. (2004). Recasting the smooth pursuit eye movement system. Journal of Neurophysiology 91:591-603.

Kunzle H, Akert K. (1977). Efferent connections of cortical, area 8 (frontal eye field) in Macaca fascicularis. A reinvestigation using the autoradiographic technique. Journal of Comparative Neurology 173:147–164.

Kunzle H, Akert K, and Wurtz RH. (1976). Projection of area 8 (frontal eye field) to superior colliculus in the monkey. An autoradiographic study. Brain Research 117:487–492.

Kuypers HG and Lawrence DG. (1967). Cortical projections to the red nucleus and the brain stem in the Rhesus monkey. Brain Research 4:151–188.

LaBerge D, Buchsbaum MS. (1990) Positron emission tomographic measurements of pulvinar activity during an attention task. Journal of Neuroscience 10:613-619.

Lau C, Zhou IY, Cheung MM, Chan KC, Wu EX. (2011). BOLD temporal dynamics of rat superior colliculus and lateral geniculate nucleus following short duration visual stimulation. PLoS ONE 6:e18914.

Li K, Patel J, Purushothaman G, Marion RT, Casagrande VA. (2013). Retinotopic maps in the puvlinar of bush baby. Journal of Comparative Neurology 521:3432-3450.

Mai JK, Paxinos G, Voss T. (2008). Atlas of the human brain. New York, NY. Academic Press.

Malpeli JG, Baker FH. (1975). The representation of the visual field in the lateral geniculate nucleus of *Macaca mulatta*. Journal of Comparative Neurology 161:569-594.

Marrocco RT, Li RH. (1977) Monkey superior colliculus: properties of single cells and their afferent inputs. Journal of Neurophysiology 40:844-860.

Mathers LH, Rapisardi SC. (1973). Visual and somatosensory receptive fields of neurons in the squirrel monkey pulvinar. Brain Research 64:65-83.

McAlonan K, Cavanaugh J, Wurtz RH. (2006). Attentional modulation of thalamic reticular neurons. Journal of Neuroscience 26:4444-4450.

Merabet L, Desautels A, Minville K, Casanova C. (1998). Motion integration in a thalamic visual nucleus. Nature 396:265-268.

Montero VM, Guillery RW, and Woolsey CN. (1977). Retinotopic organization within the thalamic reticular nucleus demonstrated by a double label autoradiographic technique. Brain Research 138:407–421.

Moschovakis AK, Scudder CA, Highstein SM. (1996). The microscopic anatomy and physiology of the mammalian saccadic system. Progress in Neurobiology 50:133-254.

Pelli DG. (1997). The VideoToolbox software for visual psychophysics: transforming numbers into movies. Spatial Vision: 10:437-442.

Petersen SE, Robinson DL, Keys W. (1985). Pulvinar nuclei of the behaving rhesus monkey: visual responses and their modulation. Journal of Neurophysiology 54:867-886.

Pinault D, Bourassa J, and Deschênes M. (1995b). Thalamic reticular input to the rat visual thalamus: a single fiber study using biocytin as an anterograde tracer.Brain Research 670:147–152.

Polyak S. (1953). Santiago Ramon y Cajal and his investigation of the nervous system. Journal of Comparative Neurology 98:3-8.

Schiller PH, Koerner F. (1971) Discharge characteristics of single units in superior colliculus of the alert rhesus monkey. Journal of Neurophysiology 34:920-936.

Schiller PH, Stryker M. (1972) Single-unit recording and stimulations in superior colliculus of the alert rhesus monkey. Journal of Neurophysiology 35:915-924.

Schneider KA, Richter MC, Kastner S. (2004). Retinotopic organization and functional subdivisions of the human lateral geniculate nucleus: a high-resolution functional magnetic resonance imaging study. Journal of Neuroscience 24:8975-8985.

Schneider KA, Kastner S. (2005). Visual responses of the human superior colliculus: a high-resolution functional magnetic resonance imaging study. Journal of Neurophysiology 94:2941-2503.

Schneider KA, Kastner S. (2009). Effects of sustained spatial attention in the human lateral geniculate nucleus and superior colliculus. Journal of Neuroscience 29:1784-1795.

Schneider K. (2011). Subcortical mechanisms of feature-based attention. Journal of Neuroscience 31:8643-8653.

Sherman SM, Guillery RW. (1996). Functional organization of thalamocortical organization. Journal of Neurophysiology 76:1367-1395.

Smith AT, Cotton PL, Bruna A, Moutsiana C. (2009). Dissociating vision and visual attention early in the visual pathway. Neuron 42:155-162.

Smith AT, Singh KD, Williams AL, Greenlee MW. (2001). Estimating receptive field size from fMRI data in human striate and extrastriate visual cortex. Cerebral Cortex 11:1182-1190.

Sparks DL. (1986). Translation of sensory signals into commands for control of saccadic eye movements: role of primate superior colliculus. Physiological Review 66:118-171.

Sparks DL. (2002). The brainstem control of saccadic eye movements. Nature Reviews Neuroscience 3: 952-964.

Tseng, KY, Riquelme LA, Belforte JE, Pazo JH, Murer MG. (2000). Substantia nigra pars reticulata units in 6-hydroxydopamine-lesioned rats: Responses to striatal D2 dopamine receptor stimulation and s subthalamic lesions. European Journal of Neuroscience 12: 247-256.

Ungerleider LG, Desimone R, Galkin TW, Mishkin M. (1984) Subcortical projections of area MT in the macaque. Journal of Comparative Neurology 223:368-386.

Viviano JD, Schneider KA. (2015). Interhemispheric interactions of the human thalamic reticular nucleus. Journal of Neuroscience (In Press).

Wilson ME, Toyne MJ. (1970). Retinotectal and corticotectal projections in macaca mulatta. Brain Research 24: 395-406.

Wang S, Bickford ME, van Horn SC, Erisir A, Godwin DW, and Sherman SM. (2001). Synaptic targets of thalamic reticular nucleus terminals in the visual thalamus of the cat. Journal of Comparitive Neurology 440:321–341.

Worsley KJ, Liao CH, Aston J, Petre V, Duncan GH, Morales F, Evans AC. (2002). A general statistical analysis for fMRI data. NeuroImage 15:1-15.

Wurtz RH, Albano JE. (1980). Visual-motor function of the primate superior colliculus. Annual Review of Neuroscience 3: 189-226.

Xu X, Ichida JM, Allison JD, Boyd JD, Bonds AB, Casagrande VA. (2001). A comparison of koniocellular receptive field properties in the lateral geniculate nucleus of the owl monkey (Aotus trivirgatus). Journal of Physiology 531:202-218.

Xu X, Bonds AB, Casagrande VA. (2002). Modeling receptive-field structure of koniocellular, magnocellular, and parvocellular cells in the owl monkey (Aotus trivirgatus). Visual Neuroscience 19:703-711.